ANNUAL REVIEWS

Annual Review of Fluid Mechanics

Turbulent Rotating Rayleigh–Bénard Convection

Robert E. Ecke[1,2] and Olga Shishkina[3]

[1]Center for Nonlinear Studies, Los Alamos National Laboratory, Los Alamos, New Mexico, USA; email: ecke@lanl.gov

[2]Department of Physics, University of Washington, Seattle, Washington, USA

[3]Max Planck Institute for Dynamics and Self-Organization, Göttingen, Germany; email: Olga.Shishkina@ds.mpg.de

Annu. Rev. Fluid Mech. 2023. 55:603–38

First published as a Review in Advance on October 20, 2022

The *Annual Review of Fluid Mechanics* is online at fluid.annualreviews.org

https://doi.org/10.1146/annurev-fluid-120720-020446

Keywords

turbulence, buoyancy, rotation, convection, Rayleigh–Bénard flow, heat transport, theory, measurements, direct numerical simulations

Abstract

Rotation with thermally induced buoyancy governs many astrophysical and geophysical processes in the atmosphere, ocean, sun, and Earth's liquid-metal outer core. Rotating Rayleigh–Bénard convection (RRBC) is an experimental system that has features of rotation and buoyancy, where a container of height H and temperature difference Δ between its bottom and top is rotated about its vertical axis with angular velocity Ω. The strength of buoyancy is reflected in the Rayleigh number ($\sim H^3\Delta$) and that of the Coriolis force in the Ekman and Rossby numbers ($\sim\Omega^{-1}$). Rotation suppresses the convective onset, introduces instabilities, changes the velocity boundary layers, modifies the shape of thermal structures from plumes to vortical columns, affects the large-scale circulation, and can decrease or enhance global heat transport depending on buoyant and Coriolis forcing. RRBC is an extremely rich system, with features directly comparable to geophysical and astrophysical phenomena. Here we review RRBC studies, suggest a unifying heat transport scaling approach for the transition between rotation-dominated and buoyancy-dominated regimes in RRBC, and discuss non-Oberbeck–Boussinesq and centrifugal effects.

1. INTRODUCTION TO ROTATING RAYLEIGH–BÉNARD CONVECTION

RRBC: Rotating Rayleigh–Bénard convection

RBC: Rayleigh–Bénard convection

Rotating Rayleigh–Bénard convection (RRBC) (Chandrasekhar 1953, Nakagawa & Frenzen 1955, Veronis 1959, Rossby 1969, Lucas et al. 1983, Boubnov & Golitsyn 1986, Zhong et al. 1993, Boubnov & Golitsyn 1995, Julien et al. 1996, Knobloch 1998, Hart et al. 2002, Vorobieff & Ecke 2002, Stevens et al. 2013, Kunnen 2021) is considerably more complex than its nonrotating counterpart (Ahlers et al. 2009b). Instead of three dimensionless control parameters in classical Rayleigh–Bénard convection (RBC)—the Rayleigh number $\mathcal{R}a$, the Prandtl number $\mathcal{P}r$, and the container geometry, represented by its aspect ratio Γ—there are two additional parameters in RRBC, the rotation rate in the Ekman number $\mathcal{E}k$ (alternatively, the Taylor number $\mathcal{T}a$ or convective Rossby number $\mathcal{R}o$), and centrifugal acceleration in the Froude number $\mathcal{F}r$ (see the sidebar titled Dimensionless Quantities in RRBC). Some of the complexity of RRBC comes from the presence of two linear instabilities associated with the onset of convection: one from the conductive state to convection in the bulk for a laterally infinite system (Chandrasekhar 1953) and another occurring at smaller $\mathcal{R}a$ to a state of traveling wall modes localized near the vertical boundaries of the container (Rossby 1969, Buell & Catton 1983, Pfotenhauer et al. 1987, Zhong et al. 1991, Ecke et al. 1992). Another important feature of bulk RRBC is that the nonlinear state is subject to a nonlinear instability [e.g., the Küppers–Lortz instability (Küppers & Lortz 1969, Cox & Matthews 2000)] so that the observed states of bulk convection even near onset are always time dependent (e.g., Zhong et al. 1993, Ning & Ecke 1993). Finally, there is a regime of quasi-geostrophic convection and geostrophic turbulence [Boubnov & Golitsyn 1986; Sakai 1997; Sprague et al. 2006; Julien et al. 2012a,b; Kunnen 2021] where in the limit of rapid rotation the Coriolis force is dominantly balanced by the pressure gradient. This regime is associated with astrophysical and geophysical flows (Pedlosky 1987, Glatzmaier 2014).

RRBC has enjoyed a renaissance in the past decade, with numerous advances on theoretical, experimental, and numerical fronts. This review aims to sort out the main complexities in

DIMENSIONLESS QUANTITIES IN RRBC

Dimensionless Control Parameters in RRBC

Rayleigh number: $\mathcal{R}a \equiv \tau_\kappa \tau_\nu / \tau_{\rm ff}^2 = \alpha g \Delta H^3/(\kappa\nu)$, the ratio of buoyancy to diffusion
Critical Rayleigh number for onset of bulk convection: $\epsilon \equiv \widetilde{\mathcal{R}a} - 1$, with $\widetilde{\mathcal{R}a} \equiv \mathcal{R}a/\mathcal{R}a_{\rm c}$
Prandtl number: $\mathcal{P}r \equiv \tau_\kappa/\tau_\nu = \nu/\kappa$, the ratio of momentum diffusion to heat diffusion
Ekman number: $\mathcal{E}k \equiv \tau_\Omega/\tau_\nu = \nu/(2\Omega H^2)$, the ratio of viscous to Coriolis forces
Taylor number: $\mathcal{T}a \equiv (\tau_\nu/\tau_\Omega)^2 = \mathcal{E}k^{-2}$, the ratio of Coriolis to viscous forces (an alternative to $\mathcal{E}k$)
Rossby number: $\mathcal{R}o \equiv \tau_\Omega/\tau_{\rm ff} = \mathcal{E}k\sqrt{\mathcal{R}a/\mathcal{P}r}$, the ratio of buoyancy to rotation
Froude number: $\mathcal{F}r \equiv (\tau_{\rm ff}/\tau_{\rm c})^2\Gamma/2 = \Omega^2 R/g$, the ratio of centrifugal to gravitational forces
Centrifugal Rossby number: $\mathcal{R}o_{\rm c} \equiv \tau_\Omega/\tau_{\rm c} = \sqrt{\alpha\Delta}/2$, the ratio of centrifugal to Coriolis forces
Aspect ratio: $\Gamma \equiv D/H$, the ratio of diameter to height of a cylindrical convection cell

Dimensionless Global Response Quantities in RRBC

Reynolds number: $\mathcal{R}e \equiv \tau_\nu/\tau_{\rm i} = UH/\nu$, the ratio of inertia to momentum diffusion
Nusselt number: $\mathcal{N}u \equiv q/q_0$, the ratio of total to conductive heat flux; in the Oberbeck–Boussinesq case, $\mathcal{N}u = (\langle u_z T\rangle_z - \kappa\partial_z\langle T\rangle_z)/(\kappa\Delta/H)$, with $\langle\cdot\rangle_z$ time average over cross sections at height z; $\mathcal{N}u_0$ is the Nusselt number in nonrotating RBC for given $\mathcal{R}a$ and fluid and container properties

turbulent RRBC and put the subject on a firm foundation. For that purpose, we confine our review to RRBC with $\mathcal{Pr} > 0.7$ and leave out the very interesting topics of open-surface flows (e.g., Boubnov & Golitsyn 1986, Fernando et al. 1991, Bouillaut et al. 2021), convection in spherical geometry (Aurnou & Olson 2001, Busse 2002, Gastine et al. 2016, Guervilly & Cardin 2016, Kaplan et al. 2017, Long et al. 2020, Wang et al. 2021), and oscillatory convection for low-$\mathcal{Pr}$ fluids, applicable to liquid metals that constitute the Earth's outer core and the plasma in the convective zone of stars (e.g., see Chandrasekhar 1953, Zhang & Roberts 1997, Aurnou et al. 2018, Grannan et al. 2022). We also do not discuss the traveling wave modes of RRBC (Zhong et al. 1991, Ecke et al. 1992, Goldstein et al. 1993, Herrmann & Busse 1993, Kuo & Cross 1993) associated with the instability at $\mathcal{Ra} < \mathcal{Ra}_c$, except with regard to their influence on the bulk convective state. Finally, we concentrate on results for intermediate $\mathcal{Pr} \approx 7$, owing to the large amount of data obtained in experiments using water. We also mention results for $\mathcal{Pr} \approx 1$ where geostrophic turbulence seems to be most accessible (Julien et al. 2012b).

OB: Oberbeck–Boussinesq

BC: boundary condition

In this section we formulate the governing equations in the Oberbeck–Boussinesq (OB) approximation, introduce control and response parameters, and summarize the theoretical framework and the overall experimental-numerical characteristics of RRBC. Sections 2 and 3 focus on, respectively, the global flow structures and heat and momentum transport in different regimes of RRBC. In Section 4 we discuss RRBC configurations that deviate from the classical OB case, including the influence of strong centrifugation and different boundary conditions (BCs). We conclude with a discussion of open questions in RRBC and give an outlook on the experimental and numerical studies desired to better understand geostrophic turbulence in RRBC and in astro- and geophysical flows.

1.1. Governing Equations and Parameters

With a change of coordinate system from stationary to one rotating with angular velocity $\mathbf{\Omega} = \Omega \boldsymbol{e}_z$, additional Coriolis ($-2\mathbf{\Omega} \times \mathbf{u}$) and centrifugal ($-\mathbf{\Omega} \times \mathbf{\Omega} \times \mathbf{r}$) accelerations occur as additional effective body-force terms in the momentum equation:

$$\partial_t \mathbf{u} + (\mathbf{u} \cdot \nabla)\mathbf{u} = -\nabla P/\rho + \nu \nabla^2 \mathbf{u} + \mathbf{g} - 2\mathbf{\Omega} \times \mathbf{u} - \mathbf{\Omega} \times \mathbf{\Omega} \times \mathbf{r} \qquad 1.$$

(for notational conventions, see the sidebar titled Dimensional Characteristics of RRBC). For $\mathbf{\Omega} \equiv \Omega \boldsymbol{e}_z$ one obtains $-\mathbf{\Omega} \times \mathbf{\Omega} \times \mathbf{r} = \Omega^2 r \boldsymbol{e}_r$.

In the simplest OB approximation that admits buoyancy (Oberbeck 1879, Boussinesq 1903), all fluid properties are assumed to be constant except for the density in the buoyancy term, where it is taken to be linearly dependent on temperature, $\rho \approx \rho_0[1 - \alpha(T - T_0)]$. Introducing the reduced pressure, $p \equiv P + \rho_0 g z \boldsymbol{e}_z - (\rho_0/2)\Omega^2 r^2 \boldsymbol{e}_r$, from $|\alpha(T - T_0)| \leq \alpha\Delta/2 \ll 1$, which holds in the OB approximation, we obtain $P/\rho \approx (P/\rho_0)[1 + \alpha(T - T_0)]$, as well as the momentum equation in the OB approximation (e.g., Becker et al. 2006),

$$\partial_t \mathbf{u} + (\mathbf{u} \cdot \nabla)\mathbf{u} = -\nabla p/\rho_0 + \nu \nabla^2 \mathbf{u} - 2\Omega \boldsymbol{e}_z \times \mathbf{u} - \alpha(T - T_0)\Omega^2 r \boldsymbol{e}_r + \alpha(T - T_0) g \boldsymbol{e}_z, \qquad 2.$$

which together with the continuity equation, $\nabla \cdot \mathbf{u} = 0$, and the heat equation,

$$\partial_t T + (\mathbf{u} \cdot \nabla) T = \kappa \nabla^2 T, \qquad 3.$$

form the governing equations in OB RRBC. One can see from the last two terms in Equation 2 that for RRBC there is gravitational buoyancy that acts in the vertical direction (as in nonrotating RBC)

DIMENSIONAL CHARACTERISTICS OF RRBC

Buoyancy timescale: $\tau_{\mathrm{ff}} \equiv H/u_{\mathrm{ff}}$
Viscous timescale: $\tau_\nu \equiv H^2/\nu$
Thermal timescale: $\tau_\kappa \equiv H^2/\kappa$
Coriolis timescale: $\tau_\Omega \equiv 1/(2\Omega)$
Centrifugal timescale: $\tau_{\mathrm{c}} \equiv 1/(\sqrt{\alpha\Delta}\Omega)$
Inertial timescale: $\tau_{\mathrm{i}} \equiv H/U$, with U the reference velocity
Velocity field: $\mathbf{u} \equiv (u_r, u_\phi, u_z)$, with radial $\boldsymbol{e}_r$, azimuthal $\boldsymbol{e}_\phi$, and vertical $\boldsymbol{e}_z$ components
Convective free-fall velocity: $u_{\mathrm{ff}} \equiv \sqrt{\alpha g \Delta H}$
Pressure: P, with $p \equiv P + \rho_0 g z \boldsymbol{e}_z - (\rho_0/2)\Omega^2 r^2 \boldsymbol{e}_r$ the reduced pressure
Temperature: T, with $T = T_+$ ($T = T_-$) at the bottom (top), $\Delta \equiv T_+ - T_-$, $T_0 \equiv (T_+ + T_-)/2$
Total vertical heat flux per unit area: q, with $q_0 \equiv C_{\mathrm{p}}\kappa\rho\Delta/H$ the heat flux from conduction
Density: ρ, with $\rho \approx \rho_0[1 - \alpha(T - T_0)]$ in the buoyancy term in the Oberbeck–Boussinesq approximation
Isobaric thermal expansion coefficient: α
Specific heat capacity: C_{p}
Kinematic viscosity of the fluid: ν
Thermal diffusivity of the fluid: κ
Angular velocity: $\boldsymbol{\Omega} \equiv \Omega \boldsymbol{e}_z$, with Ω the angular rotation rate
Gravity vector: $\mathbf{g} \equiv -g\boldsymbol{e}_z$, with g acceleration of gravity

but also centrifugal buoyancy that acts in the radial direction and can only be neglected if Ω is small. Note that in several textbooks, including that of Chandrasekhar (1961), the centrifugal term is evaluated under the assumption that the density is constant, which allows one to put the whole centrifugal term into the reduced pressure and thus leads to an equation similar to Equation 2, but without the last term. To study the centrifugal effects within the OB approximation, however, one needs to consider the full momentum Equation 2 (as in, e.g., Becker et al. 2006; Marques et al. 2007; Lopez & Marques 2009; Scheel et al. 2010; Horn & Aurnou 2018, 2019, 2021). The standard BCs for Equations 2 and 3 are no slip for the velocity ($\mathbf{u} = 0$) at all walls, isothermal temperature at the bottom (T_+) and top ($T_- < T_+$), and adiabatic ($\partial T/\partial \mathbf{n} = 0$) at the sidewall.

Flow dynamics, global structures, and scaling relations of the heat and momentum transport in RRBC are determined by the dimensionless control parameters (see the sidebar titled Dimensionless Quantities in RRBC), which can be understood as ratios of involved forces or as ratios of related timescales. The dominance of one force over others determines transitions from one regime to another. These control parameters or suitable combinations occur explicitly in the corresponding dimensionless governing equations, which depend on the choice of the reference quantities. For example, taking as the reference quantities $H/\sqrt{\alpha g \Delta H}$ for time, Δ for temperature, H for length, $\sqrt{\alpha g \Delta H}$ for velocity, and $\rho_0 \alpha g \Delta H$ for the reduced pressure, one obtains dimensionless equations that look similar to Equations 2 and 3, but with the following substitutions for the viscosity $\nu \to \sqrt{\mathcal{P}r/\mathcal{R}a}$, the thermal diffusivity $\kappa \to 1/\sqrt{\mathcal{P}r\mathcal{R}a}$, the reduced pressure term $\nabla p/\rho_0 \to \nabla p$, the Coriolis force term $2\Omega \boldsymbol{e}_z \times \mathbf{u} \to \mathcal{R}o^{-1}\boldsymbol{e}_z \times \mathbf{u}$, the gravitational buoyancy term $\alpha(T - T_0)g \to T$, and the centrifugal buoyancy term $\alpha(T - T_0)\Omega^2 r\boldsymbol{e}_r \to (2\mathcal{F}r/\Gamma)\, T\, r\boldsymbol{e}_r$. Comparing the dimensionless gravitational and centrifugal buoyancy terms, one concludes that the latter, $-\alpha(T - T_0)\Omega^2 r\boldsymbol{e}_r$, is negligible for $\mathcal{F}r \ll 1$. In the following, we focus on the case of $\mathcal{F}r \ll 1$ but return to the influence of centrifugation in Section 4.

1.2. Theoretical Background, Main Features, and Scaling Properties

There are several perspectives that one may adopt for describing turbulent RRBC. The first is to treat the system in the rotation-dominated limit beginning at the onset of convection, where the Taylor–Proudman constraint and quasi-geostrophy play major roles, and to increase the effect of buoyancy until it becomes dominant (i.e., maintain constant $\mathcal{E}k$ while increasing $\mathcal{R}a$). The second is to perturb the buoyancy-dominated state of turbulence by increasing rotation (decreasing $\mathcal{E}k$) at constant $\mathcal{R}a$. We discuss both here but take as a starting point the rotation-dominated limit because the major elements of RRBC—rotational suppression of convection, Taylor–Proudman constraint, Ekman boundary layer (BL), quasi-geostrophic convection, etc.—arise from that perspective.

BL: boundary layer

1.2.1. Onset of bulk convection, nonhydrostatic quasi-geostrophic balance, and the Taylor–Proudman constraint. Rotation postpones the onset of convection in the bulk of the domain. Linear stability analysis (Chandrasekhar 1953, Niiler & Bisshopp 1965, Homsy & Hudson 1971) shows that bulk convection sets in at a critical $\mathcal{R}a = \mathcal{R}a_c$ in the form of either steady or oscillatory flow, depending on $\mathcal{P}r$:

$$\mathcal{R}a_c \approx \begin{cases} \left(3 \times 2^{-2/3}\pi^{4/3} - 2^{13/6}\pi^{2/3}\mathcal{E}k^{1/6}\right)\mathcal{E}k^{-4/3} \approx 8.7\mathcal{E}k^{-4/3}, & \mathcal{P}r \gtrsim 0.68 \text{ (steady)}, \\ 3 \times 2^{1/3}\pi^{4/3}\frac{\mathcal{P}r^{4/3}}{(1+\mathcal{P}r)^{1/3}}\mathcal{E}k^{-4/3} \approx 17.4\frac{\mathcal{P}r^{4/3}}{(1+\mathcal{P}r)^{1/3}}\mathcal{E}k^{-4/3}, & \mathcal{P}r \lesssim 0.68 \text{ (oscillatory)}, \end{cases} \qquad 4.$$

where a reduction of $2^{13/6}\pi^{2/3}\mathcal{E}k^{1/6}$ in the large-$\mathcal{P}r$ case is a correction for no-slip BCs at the plates (see also Homsy & Hudson 1971). The onset of bulk convection in the form of a steady flow is preferred for $1 + \mathcal{P}r < 8\mathcal{P}r^4$ (i.e., for $\mathcal{P}r \gtrsim 0.6766 \approx 0.68$).

For rapid rotation ($\mathcal{E}k \to 0$) there is approximate geostrophic balance between Coriolis and pressure-gradient terms in Equation 1 (Boubnov & Golitsyn 1986, Sakai 1997, Sprague et al. 2006, Julien et al. 2012b, King & Aurnou 2013, Aurnou et al. 2020, Aguirre Guzmán et al. 2021). Taking the curl of geostrophic balance, for an incompressible flow and $\boldsymbol{\Omega} = \Omega \boldsymbol{e}_z$ with a constant Ω, one derives $0 \approx \boldsymbol{\nabla} \times (\boldsymbol{\Omega} \times \mathbf{u}) \approx -(\boldsymbol{\Omega} \cdot \boldsymbol{\nabla})\mathbf{u}$ and, hence, the result $\partial \mathbf{u}/\partial z = 0$, which is known as the Taylor–Proudman constraint (Taylor 1921, Proudman 1916). In order to sustain convective vertical motion, this constraint must be broken in cells of finite vertical extent. Nevertheless, the constraint gives an intuitive sense of the suppression of the onset of convection and the strong anisotropy between lateral and vertical length scales and timescales, as quantified below. Owing to convection, the vertical force balance is nonhydrostatic and the lateral balance has smaller-order nongeostrophic contributions leading to a state of approximate or quasi-geostrophy. We denote the asymptotic description (Sprague et al. 2006, Julien et al. 2012b) of RRBC in the rapidly rotating limit as nonhydrostatic quasi-geostrophic. A recent numerical study of the force balance in RRBC (Aguirre Guzmán et al. 2021) quantifies the quasi-geostrophic balance for a considerable region above the onset of convection in both the interior and BLs, with nongeostrophic forces contributing at around the 10% level. Reflecting the high degree of vertical to horizontal anisotropy, the length scale in the vertical direction at the onset of convection is the height H, whereas the horizontal length is ℓ_c (1/2 the critical wavelength), given by

$$\frac{\ell_c}{H} \approx \begin{cases} 2^{1/6}\pi^{2/3}\mathcal{E}k^{1/3} \approx 2.4\mathcal{E}k^{1/3}, & \mathcal{P}r \gtrsim 0.68, \\ 2^{1/6}\pi^{2/3}(1+\mathcal{P}r^{-1})^{1/3}\mathcal{E}k^{1/3} \approx 2.4(1+\mathcal{P}r^{-1})^{1/3}\mathcal{E}k^{1/3}, & \mathcal{P}r \lesssim 0.68. \end{cases} \qquad 5.$$

This is obtained from linear stability analysis for Cartesian (Chandrasekhar 1953) or cylindrical systems under the assumption that the first unstable mode is, respectively, a single normal mode or a single mode of the form $\sim J_n(kr)\cos(n\phi)\sin(\pi z/H)\exp(i\omega_0 t)$ (e.g., see Goldstein et al. 1993)

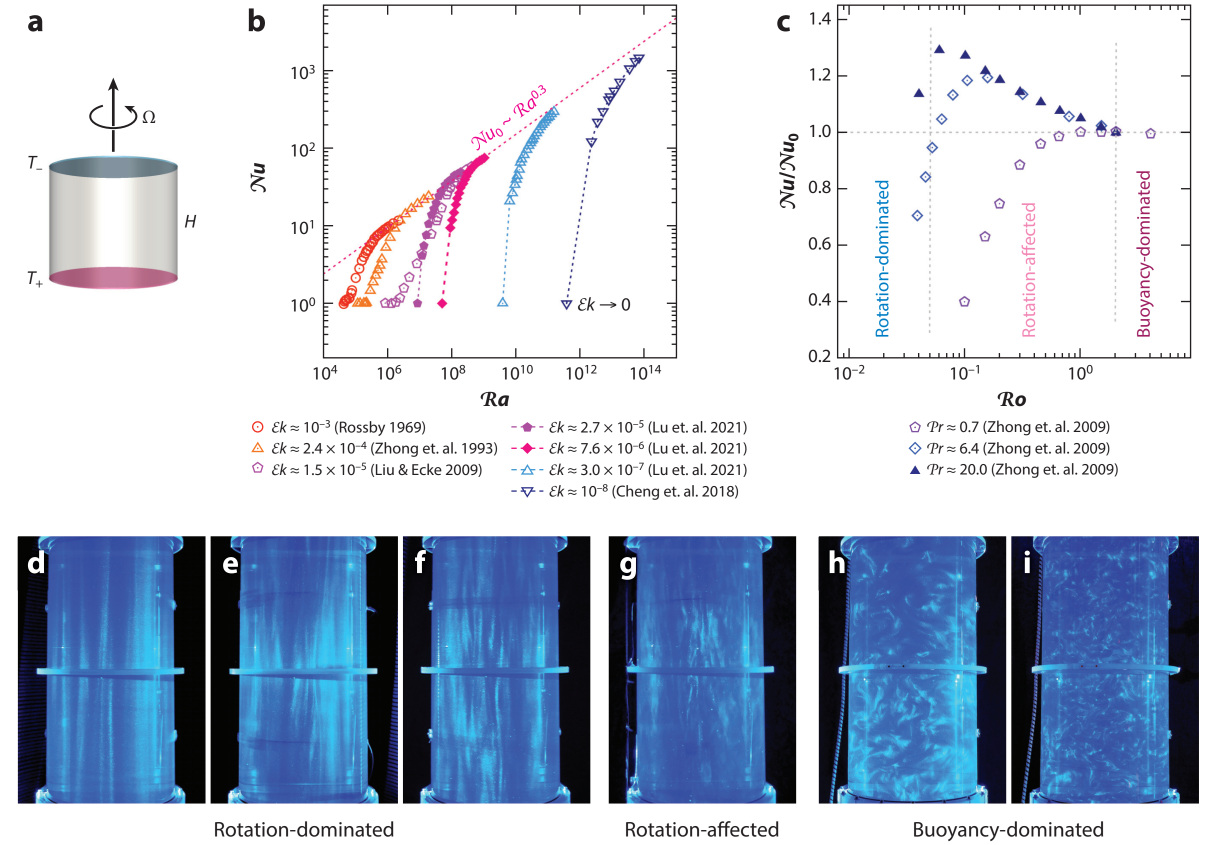

Figure 1

(*a*) An RRBC setup: A container of height H is filled with a fluid and rotated about a vertical axis at angular rate Ω. The bottom (top) is kept at temperature T_+ (T_-) with $T_- < T_+$. (*b*) $\mathcal{N}u$ versus $\mathcal{R}a$ for experimental runs at constant $\mathcal{E}k$ and $\mathcal{P}r \approx 7$. The right arrow indicates decreasing $\mathcal{E}k$. The Nusselt number in the nonrotating case, $\mathcal{N}u_0 \sim \mathcal{R}a^{0.3}$, is labeled with small differences in $\mathcal{N}u_0$ for each data set. (*c*) $\mathcal{N}u/\mathcal{N}u_0$ versus $\mathcal{R}o$ for runs at constant $\mathcal{R}a \approx 10^8$. (*d–i*) Experimental images (Cheng et al. 2020) showing representative examples of (*d–f*) rotation-dominated, (*g*) rotation-affected, and (*h–i*) buoyancy-dominated or nonrotating states. Panels *d–i* adapted from Cheng et al. (2020) with permission; copyright 2020 American Physical Society.

(J_n is the Bessel function of the first kind). For large $\Gamma \equiv D/H \gg 1$, one obtains (Shishkina 2021) the relations of Equations 4 and 5 in the limit $\mathcal{E}k(1+\mathcal{P}r)/\mathcal{P}r \to 0$. In the steady case we have $\omega_0 = 0$, whereas in the oscillatory case, the oscillation frequency ω_0 in the same limit $\mathcal{E}k/\mathcal{P}r \to 0$ follows $|\omega_0|/\Omega = [2\pi/(1+\mathcal{P}r)]^{2/3}\mathcal{P}r^{-1/3}(2-3\mathcal{P}r^2)^{1/2}\,\mathcal{E}k^{1/3}$.

1.2.2. Main features.

An overview of the features of RRBC starting at onset can be seen in heat transport ($\mathcal{N}u$) measurements, covering almost 10 (5) decades in $\mathcal{R}a$ ($\mathcal{E}k$) using water with $\mathcal{P}r \approx 7$ (see **Figure 1*b***). The rapid rise from the conduction value $\mathcal{N}u = 1$ represents the nonlinear growth from onset and defines a region of rotation-dominated quasi-geostrophic dynamics with intrinsic time dependence arising from nonlinear instability (Küppers & Lortz 1969, Cox & Matthews 2000) at any $\mathcal{R}a > \mathcal{R}a_c$. As demonstrated by these data, the range of $\mathcal{N}u$ spanned in this region increases with decreasing $\mathcal{E}k$ so that in the limit $\mathcal{E}k \to 0$, the buoyancy-dominated state becomes out of reach. In this limit, one can write a system of nonhydrostatic quasi-geostrophic equations valid asymptotically as $\mathcal{E}k \to 0$, $\mathcal{R}o \to 0$, and $\mathcal{R}a \to \infty$ such that $\widetilde{\mathcal{R}a} \equiv \mathcal{R}a/\mathcal{R}a_c \sim \mathcal{E}k^{4/3}\mathcal{R}a$ remains finite (Sprague et al. 2006, Julien et al. 2012b). This approach holds promise to bridge to geo- and astrophysical systems with extreme values of $\mathcal{Ra}$ and $\mathcal{Ek}$ and provides a theoretical framework for describing the evolution of states in the rotation-dominated regime, often called the geostrophic regime, in which states of cellular flows, Taylor columns, plumes, and geostrophic turbulence are seen in experiments and solutions of the reduced equations (see **Figure 1*d–f***).

LSC: large-scale circulation

One common characteristic of the rotation-dominated regime is that thermal instability gives rise to vortical motions through the Coriolis force, $-2\mathbf{\Omega} \times \mathbf{u}$ (i.e., horizontal flows are deflected by the Coriolis force, leading to vortices). The other important element of RRBC is the altered nature of BLs. The vorticity in the interior interacts with the no-slip plates through kinetic BL of the Ekman type (Greenspan 1968, Stellmach et al. 2014, Julien et al. 2016) and can generate Ekman pumping where the interior vorticity is dissipated in the Ekman BL of thickness $\delta_{\mathrm{E}}/H \sim \mathcal{Ek}^{1/2}$, and positive (negative) vertical velocity is produced for cyclonic (anticyclonic) vorticity. In the rotation-dominated regime, the kinetic BL ($\delta_u \sim \delta_{\mathrm{E}}$) is much thinner than the thermal BL, which has a different structure from the nonrotating thermal BL, $\delta_\theta/H \approx (2\mathcal{Nu})^{-1}$, in which velocities are assumed to be small and heat is effectively carried diffusively. Owing to Ekman pumping in the rotation-dominated regime, advective processes in the thermal BL are significant so it is described as a thermal wind layer (Julien et al. 2016) to differentiate it from the nonrotating thermal BL. An important aspect of this structure is that $H/(2\delta_\theta)$ underestimates $\mathcal{Nu}$ owing to a combination of a finite mean gradient and contributions from Ekman pumping.

As $\mathcal{Ra}$ increases at constant $\mathcal{Ek}$, the balance of rotation and buoyancy shifts, as measured by increasing $\mathcal{Ro} \sim \mathcal{Ra}^{1/2}$ such that $\mathcal{Nu}$ approaches the nonrotating curve $\mathcal{Nu}_0 \sim \mathcal{Ra}^{0.3}$. For some ranges of $\mathcal{Ro}$, $\mathcal{Ra}$, and $\mathcal{Pr} \gtrsim 1$, with $\delta_u \approx \delta_\theta$ (King et al. 2009), Ekman pumping–amplified heat transport results in $\mathcal{Nu} \geq \mathcal{Nu}_0$ (e.g., Rossby 1969) (see **Figure 1*b***). For other parameter ranges (e.g., $\mathcal{Pr} \lesssim 1$ and $\mathcal{Ra} \gtrsim 10^{10}$), $\mathcal{Nu}$ is always less than $\mathcal{Nu}_0$ and asymptotes to its buoyancy-dominated dependence at some $\mathcal{Ro}_{\mathrm{t}} \gtrsim 1$ that depends on various control parameters. Thus, we identify three regimes of RRBC: rotation dominated for $\mathcal{Ro} \ll 1$, buoyancy dominated for $\mathcal{Ro} \gg 1$, and rotation affected for $\mathcal{Ro} \sim 1$. The transition from the buoyancy-dominated through the rotation-affected and into the rotation-dominated zone is well represented by increasing rotation at fixed $\mathcal{Ra}$. This approach, when normalizing by the nonrotating $\mathcal{Nu}_0$, also most readily demonstrates the enhancement of heat transport in the rotation-affected region for $\mathcal{Pr} \gtrsim 1$ and is shown in **Figure 1*c***. The different regions are indicated for this range of $\mathcal{Ra} \sim 10^8$, although, as we will see, these boundaries depend on $\mathcal{Ra}$, $\mathcal{Pr}$, and Γ as well. Characteristic experimental images in **Figure 1** show rotation-dominated (**Figure 1*d–f***), rotation-affected (**Figure 1*g***), and buoyancy-dominated (**Figure 1*h–i***) states.

1.2.3. Thermal, Ekman, and Stewartson boundary layers and Ekman pumping.

The $\mathcal{Nu}$ behaviors in different regimes of RRBC are intimately related to BLs at the top and bottom of the convection cell. In the buoyancy-dominated state, the thermal BL thickness is given by $\delta_\theta \approx H/(2\mathcal{Nu})$ and the kinetic BL is determined through the shear produced by the coherent accumulation of thermal plumes at the lateral boundaries into a large-scale circulation (LSC) (see Ahlers et al. 2009b). The resultant BL becomes thinner as the shear velocity increases with $\mathcal{Ra}$. When the system rotates sufficiently rapidly, the nature of the kinetic BL changes dramatically to an Ekman BL type. An Ekman BL is formed when a fluid in solid body rotation at angular rotation rate Ω experiences a small differential angular rotation $\Omega \pm \Delta\Omega$ ($\Delta\Omega \ll \Omega$) on a horizontal bounding surface (Greenspan 1968). In RRBC, the Ekman BL arises from the growth of thermal perturbations that lead to vertical and horizontal motion. For weak forcing with $\widetilde{\mathcal{Ra}} \sim 1$, cellular circulation takes place with cyclonic outflow away from the plates and anticyclonic reversal at the midplane (Veronis 1959, Sakai 1997) (see **Figure 2*a***). In the general case, at larger $\widetilde{\mathcal{Ra}}$ and for no-slip BCs, near the top (bottom) surface, the converging hot (cold) horizontal flow is acted upon by

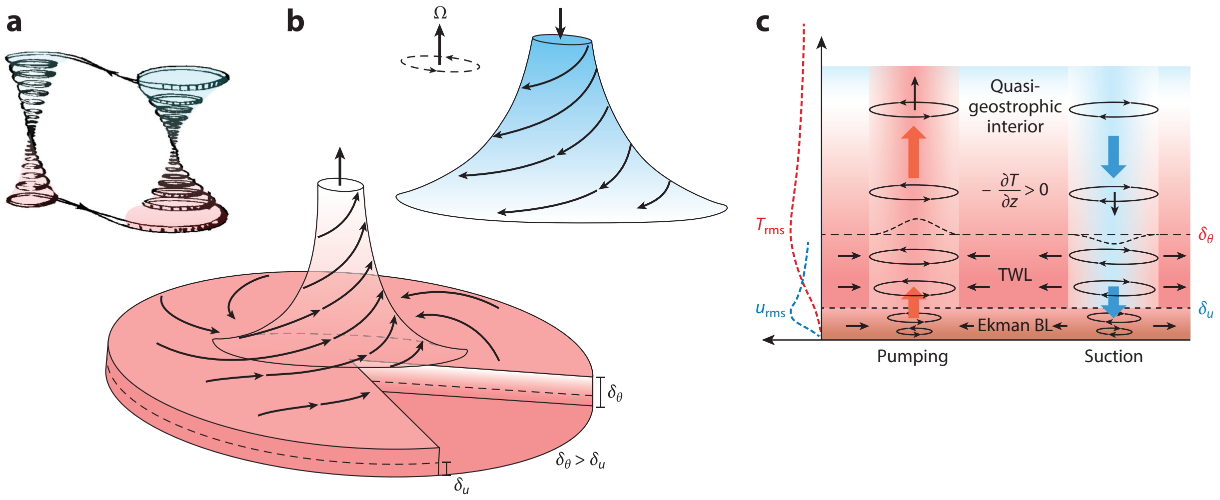

Figure 2

(*a*) Cellular flow showing fluid parcel motion with anticyclonic and cyclonic vertical vorticity that reverses sign at mid-plane. Panel adapted from Veronis (1959) with permission; copyright 1959 Cambridge University Press. (*b*) Vorticity production (not to scale). Thermal instability pulls converging warm fluid laterally into an expanding plume where it spins up cyclonically, whereas cool diverging return flow from the top (or interior) produces anticyclonic vorticity. Thermal (δ_θ) and kinetic (δ_u) boundary layer (BL) thicknesses are indicated. (*c*) Vertical profiles of BL structure. Warm (cool) upward (downward) plumes generate positive (negative) cyclonic vorticity from inflowing fluid. The vorticity produced is fairly independent of z outside of the Ekman BL and produces Ekman pumping with the vertical velocity $u_z \sim \mathcal{E}k H \omega_z$ at the distance from the plate $z = \delta_u \sim \mathcal{E}k^{1/2} H$, where ω_z is the vertical component of the vorticity and H is the cell height. Vorticity is dissipated in the Ekman BL per linear Ekman BL processes. The thermal (kinetic) BL thickness is defined by where root-mean-square (rms) temperature T_{rms} (velocity u_{rms}) is maximum with respect to z. The thermal wind layer (TWL) is in quasi-geostrophic balance with significant Ekman pumping and differs from the thermal BL in nonrotating RBC.

the Coriolis force to generate cyclonic vorticity in the rotating frame so that the local rotation rate of the fluid exceeds Ω. Similarly, the return flow from the bottom (top) to top (bottom) (where it exists for $\widetilde{\mathcal{R}a} \sim 1$) spreads out as it comes near the top (bottom) and spins down anticyclonically so that the local rotation rate is less than Ω. Thus, in both regions an Ekman BL forms with thickness $\delta_u \sim \delta_{\mathrm{E}}$ to dissipate the interior flow vorticity at the no-slip horizontal boundary. Note that, as opposed to the buoyancy dominated/nonrotating kinetic BL, the thickness of the Ekman BL only depends on $\mathcal{E}k$ and not on the strength of the velocity (i.e., on $\mathcal{R}a$). Near the onset of convection, we have $\delta_u \ll \delta_\theta$ so that Ekman pumping produces additional $u_z \sim \mathcal{E}k H \omega_z$. The vertical velocity amplification can be formulated as an effective Ekman pumping BC (Julien et al. 2016) that yields a much steeper variation of $\mathcal{N}u$ with $\widetilde{\mathcal{R}a}$ than one would expect for the rotation-dominated regime with no Ekman BL ($\mathcal{E}k \to 0$ or free-slip BCs) (Julien et al. 2012b, Stellmach et al. 2014, Plumley et al. 2016) and is consistent with measurements (Cheng et al. 2015, Lu et al. 2021) and direct numerical simulations (DNS) (Stellmach et al. 2014, Aguirre Guzmán et al. 2021).

DNS: direct numerical simulations

In the nonlinear or turbulent regime, the impact of the Ekman BL depends on its interplay with the thermal BL in a complicated manner (Julien et al. 1996, 2012b, 2016; Sprague et al. 2006; King et al. 2009; Stevens et al. 2010a; Kunnen et al. 2011, 2013; Stellmach et al. 2014; Plumley et al. 2016). **Figure 2*b*,*c*** provides a picture of Coriolis generation of vorticity and the resultant Ekman pumping process. The Ekman pumping effect is strongest for $\delta_\theta > \delta_{\mathrm{E}}$ because, in that case, Ekman pumping produces higher thermal contrast and greater thermal fluctuations. Ekman pumping also complicates the $\mathcal{N}u$:δ_θ relationship $\mathcal{N}u_\theta = H/(2\delta_\theta)$ of nonrotating RBC. For example, Aguirre Guzmán et al. (2022) showed for DNS with $\mathcal{E}k \sim 10^{-7}$ that $\mathcal{N}u \approx 2\mathcal{N}u_\theta$ over

$3 < \widetilde{\mathcal{Ra}} \lesssim 100$. Finally, Ekman pumping enhancement of $\mathcal{Nu}$ is most obvious when it results in $\mathcal{Nu} > \mathcal{Nu}_0$, where $\mathcal{Nu}_0$ is for nonrotating RBC. Numerous experimental and numerical studies have shown this enhancement effect (Rossby 1969; Julien et al. 1996; Liu & Ecke 1997, 2009; Kunnen et al. 2008; Zhong et al. 2009; Weiss et al. 2010, 2016; Schmitz & Tilgner 2010; Zhong & Ahlers 2010; Stevens et al. 2010b; Horn & Shishkina 2014; Wei et al. 2015; Rajaei et al. 2016; Chong et al. 2017; Cheng et al. 2020; Yang et al. 2020). For $\mathcal{Pr} \lesssim 1$ or $\mathcal{Ra} \gtrsim 10^{10}$, however, no or negligible $\mathcal{Nu}$ enhancement relative to $\mathcal{Nu}_0$ is observed (Niemela et al. 2010, Ecke & Niemela 2014, Stellmach et al. 2014, Horn & Shishkina 2015, Cheng et al. 2015, Wedi et al. 2021, Kunnen 2021).

BZF: boundary zonal flow

Another effect of note (Kunnen et al. 2011) is that a mean volume-averaged anticyclonic vorticity is observed to form in the interior of the cell, which implies a net Ekman suction into the BL of order $\langle u_z \rangle_{z=\delta_E} \approx (\mathcal{Ek}/2)\,\langle \omega_z \rangle H$. A global circulation model (Kunnen et al. 2013) arises from these considerations where the flow into the BLs induced by the interior anticyclonic circulation balances a flow at the vertical boundaries in the form of Stewartson BLs (Stewartson 1957, Greenspan 1968) of thickness $\propto \mathcal{Ek}^{1/3}$ (Kunnen et al. 2011, 2013). This model explained the observed layer formation but did not address the origins of the flows. Recently, however, it was demonstrated that a boundary zonal flow (BZF) (Zhang et al. 2020, 2021; de Wit et al. 2020; Wedi et al. 2021) arises over a wide range of $\mathcal{Ra}$ and $\mathcal{Ek}$ from the robustness of sidewall-traveling wall modes in the presence of bulk convection (Favier & Knobloch 2020, Ecke et al. 2022). Furthermore, the sidewall eigenfunctions for the vertical velocity of linear wall modes act mainly in the radial width that scales as $\propto \mathcal{Ek}^{1/3}$ (Herrmann & Busse 1993), in agreement with the results of Kunnen et al. (2011) and Zhang et al. (2020, 2021). Strong bulk turbulence modifies the BZF in ways still to be explored, but to first order the origin of the $\propto \mathcal{Ek}^{1/3}$ layer seems to result from the BZF as the source of vertical motion near the sidewalls with nonlinearities feeding back to produce the anticyclonic interior flow. The two descriptions seem to complement one another, with the Ekman–Stewartson mechanism feeding back on the wall mode/BZF state in a self-consistent manner. It is interesting that the wall mode vertical velocity profile, the Stewartson BL thickness, and the critical wavelength of bulk instability all scale as $\mathcal{Ek}^{1/3}$. The thermal and kinetic BLs at the plates interact to affect heat transport and other local properties of the flow. Prominent features include the finite mean temperature gradient in RRBC resulting from enhanced (decreased) lateral (vertical) mixing (e.g., Julien et al. 1996, 2012b; Hart & Ohlsen 1999; Kunnen et al. 2009; Zhong et al. 2009; Stevens et al. 2010a; Liu & Ecke 2011; King et al. 2013; Horn & Shishkina 2014) and the character of statistical moments of T, u, and ω_z.

1.2.4. Scaling properties.

Scaling relationships among measured quantities and control parameters depend on the location in RRBC parameter space and can be derived in certain limiting cases using approaches useful for nonrotating RBC. Under the assumption that the scaling relations for $\mathcal{Nu} \equiv qH/(\kappa\,\Delta)$ have the form $\mathcal{Nu} \sim \mathcal{Pr}^{\beta_0}\mathcal{Ra}^{\gamma}$ in nonrotating/buoyancy-dominated regimes and $\mathcal{Nu} \sim \mathcal{Pr}^{\beta}(\mathcal{Ra}/\mathcal{Ra}_c)^{\xi}$ in rotation-dominated regimes (for certain $\gamma > 0$ and $\xi > 0$), along with the further assumption that the dimensional heat flow q is independent of diffusion in the BLs (i.e., of κ and ν), one immediately obtains

$$\mathcal{Nu} = \mathcal{Nu}_0 \sim \mathcal{Pr}^{1/2}\mathcal{Ra}^{1/2} \quad \text{for nonrotating/buoyancy-dominated regimes,} \tag{6}$$

$$\mathcal{Nu} \sim \mathcal{Pr}^{-1/2}\mathcal{Ek}^{2}\mathcal{Ra}^{3/2} \quad \text{for the rotation-dominated regime.} \tag{7}$$

The diffusion independence of the reference velocity U, and also of H in the rotation-dominated geostrophic turbulence regime $U = \sqrt{\alpha g \Delta}/(2\Omega)$, yields

$$\mathcal{Re} = \mathcal{Re}_0 \sim \mathcal{Pr}^{-1/2}\mathcal{Ra}^{1/2} \quad \text{for nonrotating/buoyancy-dominated regimes,} \tag{8}$$

$$\mathcal{Re} \sim \mathcal{Pr}^{-1}\mathcal{Ek}\,\mathcal{Ra} \quad \text{for the rotation-dominated regime.} \tag{9}$$

Equations 6 and 8 for the buoyancy-dominated state are those of regime IV_ℓ of the Grossmann & Lohse (2000) theory for nonrotating RBC (see also Kraichnan 1962, Spiegel 1971). Equations 7 and 9 for rotation-dominated RRBC are those of the geostrophic turbulence regime (Julien et al. 2012b; also see Schmitz & Tilgner 2009). Equating the scaling relations for $\mathcal{N}u$ (or $\mathcal{R}e$) in the buoyancy-dominated and rotation-dominated regimes, one obtains that the scaling quantity is $\mathcal{R}o$. Thus, if the above assumptions are fulfilled, the transition from the buoyancy-dominated to rotation-dominated geostrophic turbulence regimes scales with $\mathcal{R}o$, $\mathcal{N}u/\mathcal{N}u_0 \sim \mathcal{R}o^2$, and $\mathcal{R}e/\mathcal{R}e_0 \sim \mathcal{R}o$ in the rotation-dominated regime and $\mathcal{N}u/\mathcal{N}u_0 \sim 1$ and $\mathcal{R}e/\mathcal{R}e_0 \sim 1$ in the buoyancy-dominated regime. The same scalings of Equations 6–9 also follow from Aurnou et al.'s (2020) approach, where relevant scales for length ℓ, velocity U, and temperature θ were introduced; the scalings $\mathcal{N}u \sim \theta U/(\kappa\Delta/H)$ and $\mathcal{R}e \sim UH/\nu$ were assumed; and terms in the vorticity equation were analyzed. For the rotation-dominated regime, Aurnou et al. (2020) proposed a balance of the Coriolis term (estimated as $2\Omega U/H$), the inertial term (U^2/ℓ^2), and the buoyancy (Archimedean) term ($g\alpha\theta/\ell$), which together with $\theta/\Delta \sim \ell/H$ lead to $U/u_{\mathrm{ff}} \sim \mathcal{R}o$, $\ell/H \sim \mathcal{R}o$ and to Equations 7 and 9 for the rotation-dominated state. For the buoyancy-dominated regime, the inertia buoyancy balances together with $\theta \sim \Delta$ and $\ell \sim H$, and $U \sim u_{\mathrm{ff}}$ leads to the scalings of Equations 6 and 8.

In other parameter ranges, different assumptions can be taken to derive scalings. Thus, assuming that q is independent not of κ and ν but of H, one derives $\mathcal{N}u \sim \mathcal{R}a^{1/3}$ for the buoyancy-dominated regime (Malkus 1954, Priestley 1959) and $\mathcal{N}u \sim (\mathcal{R}a/\mathcal{R}a_c)^3$ for the rotation-dominated state. No experimental or numerical (under realistic conditions) evidence exists, however, to support a scaling range of this latter type (also see Julien et al. 2012b). Finally we mention that a rigorous upper bound on the heat transport in RRBC derived by Grooms & Whitehead (2014), $\mathcal{N}u \leq 20.56\,\mathcal{E}k^4\mathcal{R}a^3$, is obtained from the asymptotically reduced equations for $\mathcal{E}k^{8/5}\mathcal{R}a = \mathcal{O}(1)$ in the limit of rapid rotation ($\mathcal{E}k \to 0$), strong thermal forcing ($\mathcal{R}a \to \infty$), and infinite Prandtl number. For free-slip BCs and infinite $\mathcal{P}r$, Tilgner (2022) suggests the upper bound $\mathcal{N}u < 0.144\,\mathcal{E}k^{2/3}\mathcal{R}a$. Note that the existing theoretical upper bounds are much larger than the measured ones. In Section 3 we check several hypotheses and suggest a unifying theoretical scaling model for the transition between rotation-dominated and buoyancy-dominated regimes.

1.3. Experimental and Numerical Investigations of RRBC

RRBC experiments (see examples in **Figure 3**) and DNS aim to capture a broad parameter range in the $\mathcal{R}a$–$\mathcal{E}k$ plane in order to investigate the many regimes of RRBC. These approaches are highly complementary with DNS, as they can access the full hydrodynamic fields and have the flexibility to investigate different BCs and explore combinations of control parameters that are inaccessible experimentally. Experiments, on the other hand, can easily accumulate statistical averages over much longer times, reflect realistic limitations on idealized descriptions, and access a different range of control parameters. Of particular interest is the rotation-dominated regime of very high $\mathcal{R}a$ and very small $\mathcal{E}k$, which reflects the nature of astrophysical and geophysical flows.

For a given container and a particular fluid, the range of experimental values of $\mathcal{E}k$ is restricted by the possible rotation rates Ω, and the $\mathcal{R}a$ range is restricted by the maximal and minimal temperature differences Δ that can be imposed between the bottom and top plates. The requirement to satisfy OB conditions puts additional restrictions on the imposed Δ and on the range of $\mathcal{R}a$ (Gray & Giorgini 1976, Horn & Shishkina 2014, Weiss et al. 2018) (see **Figure 4*a*** and Section 4 below). The other two demanding requirements are minimizing centrifugal effects ($\mathcal{F}r \ll 1$) and limiting the impact of vertical sidewalls so that the horizontal extent ℓ of typical structures in RRBC is much smaller than the cell diameter D (the recently discovered BZF complicates this latter criterion). Therefore, the available Ω range is bounded from above by centrifugal effects ($\mathcal{F}r \propto \Omega^2$) and from below by the cell aspect ratio Γ because of $\ell \propto \Omega^{-1/3}$ (Marques et al. 2007, Lopez &

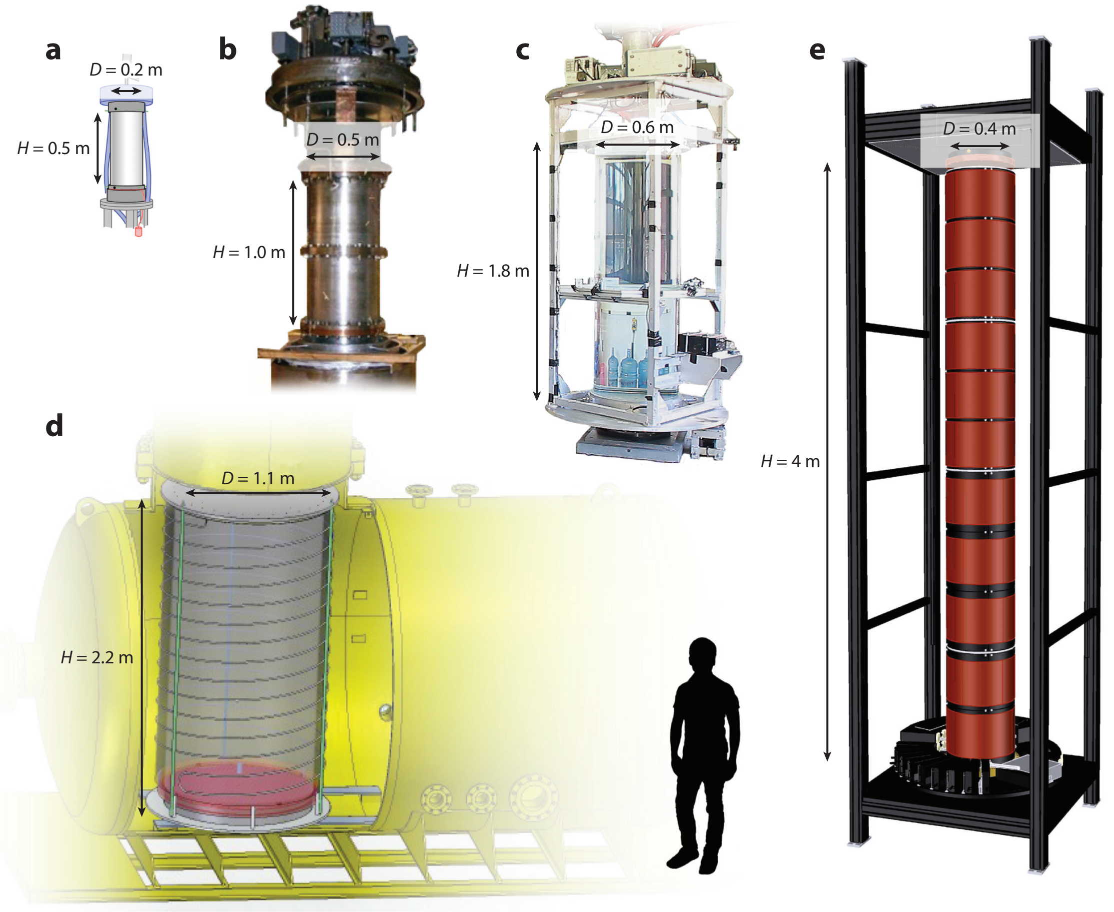

Figure 3

Examples of RRBC facilities. (*a*) RoMag (Rotating Magnetoconvection Device) at the University of California, Los Angeles (UCLA) (cell aspect ratio range $0.4 \lesssim \Gamma \lesssim 4$, liquid Ga, $0.025 \lesssim \mathcal{Pr} \lesssim 0.028$, $2.1 \times 10^{-7} \lesssim \mathcal{Ek} \lesssim 1.1 \times 10^{-4}$, $1.3 \times 10^{4} \lesssim \mathcal{Ra} \lesssim 2.2 \times 10^{9}$) (King & Aurnou 2013, Aurnou et al. 2018). (*b*) Trieste experiment at the International Centre for Theoretical Physics ($\Gamma \approx 0.5$, cryogenic liquid He, $0.69 \lesssim \mathcal{Pr} \lesssim 0.72$, $2.7 \times 10^{-7} \lesssim \mathcal{Ek} \lesssim 9.3 \times 10^{-5}$, $3.3 \times 10^{9} \lesssim \mathcal{Ra} \lesssim 1.1 \times 10^{12}$) (Niemela et al. 2000, Ecke & Niemela 2014). (*c*) NoMag (Nonmagnetic Rotating Convection Device) at UCLA ($0.11 \lesssim \Gamma \lesssim 6$, water, $3.5 \lesssim \mathcal{Pr} \lesssim 9.4$, $1.5 \times 10^{6} \lesssim \mathcal{Ra} \lesssim 9.2 \times 10^{12}$, $4.2 \times 10^{-8} \lesssim \mathcal{Ek} \lesssim 1.3 \times 10^{-3}$) (Cheng et al. 2015, Aurnou et al. 2018). (*d*) U-Boot of Göttingen at the Max Planck Institute for Dynamics and Self-Organization ($\Gamma \approx 0.5$ and $\Gamma \approx 1$; pressurized gases SF_6, N_2, and He; $0.7 \lesssim \mathcal{Pr} \lesssim 1.0$; $7.9 \times 10^{-9} \lesssim \mathcal{Ek} \lesssim 6.2 \times 10^{-1}$; $3.4 \times 10^{3} \lesssim \mathcal{Ra} \lesssim 1.2 \times 10^{15}$) (Ahlers et al. 2009a, Zhang et al. 2020, Wedi et al. 2021). (*e*) TROCONVEX (turbulent rotating convection to the extreme) at Eindhoven University of Technology ($0.1 \lesssim \Gamma \lesssim 0.5$, water, $2.1 \lesssim \mathcal{Pr} \lesssim 6.9$, $4.8 \times 10^{-9} \lesssim \mathcal{Ek} \lesssim 5.2 \times 10^{-6}$, $6.2 \times 10^{9} \lesssim \mathcal{Ra} \lesssim 2.0 \times 10^{14}$) (Cheng et al. 2018, Kunnen 2021). Figure reproduced from Cheng et al. (2018); copyright 2018 the authors (CC BY-NC-ND 4.0).

Marques 2009, Cheng et al. 2018, Horn & Aurnou 2018). The resulting parameter range in a realistic OB experiment is bounded for both $\mathcal{Ra}$ and $\mathcal{Ek}$ (see **Figure 4*b***).

DNS of RRBC are based on solving numerically nondimensionalized and discretized versions of Equations 1–3 on computational grids that are sufficiently fine in space and time to resolve the Kolmogorov and Batchelor scales within the bulk of the fluid and to provide a sufficient number of grid points to resolve velocity and temperature BLs (Shishkina et al. 2010). There are several numerical approaches: finite-volume [e.g., a fourth-order code Goldfish; see Shishkina et al.

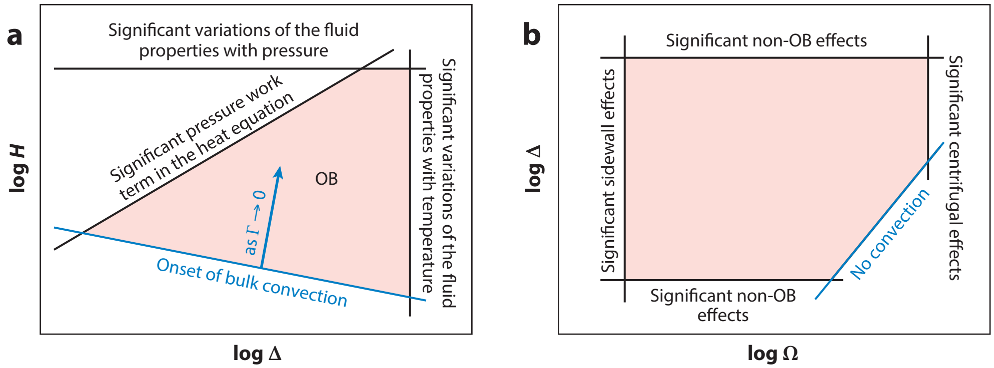

Figure 4

(*a*) Oberbeck–Boussinesq (OB) validity region in RBC in terms of the maximal temperature difference Δ and container height H, with Γ the cell aspect ratio. (*b*) Accessible range in a rotating RBC experiment with fixed H in terms of Δ and rotation rate Ω. The text near the restricting lines explains the origins of the restrictions.

(2015), Horn & Schmid (2017), Horn & Aurnou (2018, 2019, 2021), Vogt et al. (2021), Zhang et al. (2020, 2021), and Ecke et al. (2022)], finite-difference [e.g., a second-order code AFID/RBflow; see Verzicco & Camussi (2003), Stevens et al. (2009, 2010a,b, 2011, 2012), and Hartmann et al. (2022)], spectral-element [e.g., Nek5000; see Fischer (1997), Scheel (2007), and Scheel et al. (2003, 2010)], or spectral methods for periodic BCs (Stellmach & Hansen 2008, King et al. 2012) [Kooij et al. (2018) provides a code comparison].

Another method to characterize the structures and properties of the rotation-dominated regime is to asymptotically reduce the full OB RRBC equations in the limit $\mathcal{E}k \to 0$ ($\mathcal{R}o \to 0$) and $\mathcal{R}a \to \infty$ while keeping laterally periodic BCs and finite $\mathcal{E}k^{4/3}\mathcal{R}a$ (Nieves et al. 2014, Julien et al. 2016, Plumley et al. 2016, Plumley & Julien 2019). This results in nonhydrostatic quasi-geostrophic model equations that can be solved numerically.

2. FLOW STRUCTURES IN RRBC

Fluid flow organizes itself in RRBC in rich and diverse ways. We begin our discussion with the rotation-dominated regime and systematically vary control parameters to access domains with decreasing rotational influence. Taking $\mathcal{E}k$ fixed (as in **Figure 1*b***) and increasing $\mathcal{R}a$, one sequentially finds wall modes for $\mathcal{E}k^{-1} \lesssim \mathcal{R}a \lesssim \mathcal{E}k^{-4/3}$; nonhydrostatic quasi-geostrophic features of RRBC including cellular flows, convective Taylor columns, plumes, geostrophic turbulence, and large-scale vortex condensates in the range $1 \leq \widetilde{\mathcal{R}a} \lesssim 50$ to 100; the transition to the rotation-affected region with remnant spatial anisotropy and Ekman BL effects; and finally the buoyancy-dominated domain. Representative images from experiment, DNS, and the nonhydrostatic quasi-geostrophic model for each region are shown in **Figure 1*d–g*** and **Figure 5**.

The first instability to a convecting state in rotation-dominated convection is to wall modes (Zhong et al. 1991, Ecke et al. 1992, Goldstein et al. 1993, Herrmann & Busse 1993, Kuo & Cross 1993), which are confined near the sidewall, have azimuthal periodicity m, precess in a retrograde direction, and have onset at $\mathcal{R}a_{\mathrm{wm}} \approx \pi^2\sqrt{6\sqrt{3}}\mathcal{E}k^{-1}$. These states are important for considering how the system enters the quasi-geostrophic regime and undergoes a transition to turbulence owing to the surprising robustness of the wall modes as a BZF that appears to persist over the entire rotation-dominated and rotation-affected regimes (Favier & Knobloch 2020; Shishkina 2020; de Wit et al. 2020; Zhang et al. 2020, 2021; Wedi et al. 2021; Ecke et al. 2022). These states are particularly influential for small Γ, where they contribute substantially to the total heat transport.

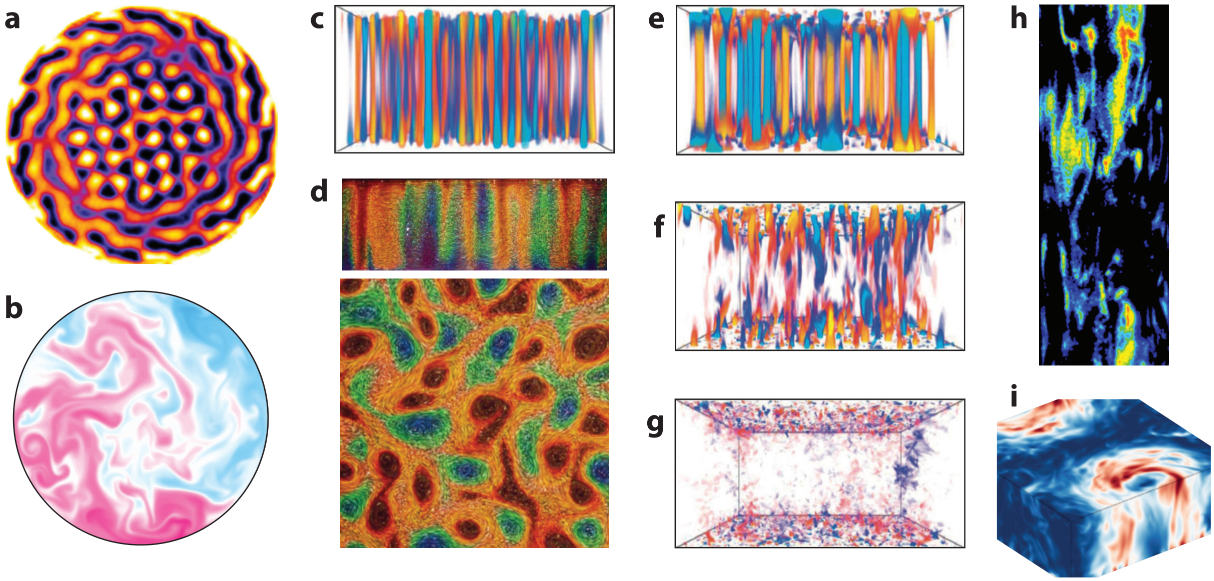

Figure 5

Representative images of RRBC flow states. (*a*) Shadowgraph image (*dark*, hot; *light*, cold) of a wall mode with mode number $m = 12$ coexisting with a bulk-state structure in the center ($\widetilde{\mathcal{R}a} \equiv \mathcal{R}a/\mathcal{R}a_c \approx 1.04$, with $\mathcal{R}a_c$ the Rayleigh number for the onset of bulk convection; $\mathcal{E}k \approx 2.3 \times 10^{-4}$; $\mathcal{P}r \approx 6.4$; and cell aspect ratio $\Gamma \approx 5$). (*b*) Temperature field from direct numerical simulations (DNS) ($\widetilde{\mathcal{R}a} \approx 5$, $\mathcal{E}k = 10^{-6}$, $\mathcal{P}r = 0.8$, $\Gamma = 1/2$). (*c*) Nonhydrostatic quasi-geostrophic volume render of temperature for the cellular state ($\widetilde{\mathcal{R}a} = 2.3$, $\mathcal{P}r = 7$). (*d*) Thermochromic liquid crystal image of the temperature field ($\widetilde{\mathcal{R}a} \approx 4$, $\mathcal{P}r \approx 7$, $\mathcal{E}k \approx 9 \times 10^{-5}$). (*e*–*g*) Volume render of temperature: (*e*) convective Taylor columns state ($\mathcal{P}r = 7$, $\widetilde{\mathcal{R}a} = 4.6$), (*f*) plume state ($\mathcal{P}r = 7$, $\widetilde{\mathcal{R}a} = 13.8$), and (*g*) nonhydrostatic quasi-geostrophic turbulence ($\mathcal{P}r = 0.7$, $\widetilde{\mathcal{R}a} = 18.4$). (*h*) Rheoscopic visualization of geostrophic turbulence ($\widetilde{\mathcal{R}a} = 77$, $\mathcal{P}r \approx 4$, $\mathcal{E}k = 1.9 \times 10^{-6}$, $\Gamma = 1/4$); the central section is shown. (*i*) Horizontal kinetic energy in the height range $0 < z/H < 3/4$ ($\mathcal{R}a = 1.7 \times 10^7$, $\mathcal{E}k = 10^{-4}$, $\mathcal{P}r = 1$) from DNS. Panels adapted with permission from (*a*) Ning & Ecke (1993), (*c*, *e*–*g*) Julien et al. (2012b), (*d*) Sakai (1997), (*h*) Cheng et al. (2015), and (*i*) de Wit et al. (2022).

2.1. Quasi-Geostrophic Convection

Several states of RRBC have been identified using the nonhydrostatic quasi-geostrophic approach (Sprague et al. 2006, Julien et al. 2012b). Near onset, RRBC takes the form of cellular vortical structures (Chandrasekhar 1953, Veronis 1959) (see Equations 4 and 5 and **Figure 2*a***). These structures (**Figure 5*a*,*c*,*d***) are nonlinearly unstable to slow dynamics (Küppers & Lortz 1969, Cox & Matthews 2000). With increasing $\widetilde{\mathcal{R}a}$ and $\mathcal{P}r \gtrsim 3$, the flow structures gradually change to convective Taylor columns (**Figure 1*d*** and **Figure 5*e***) with an interesting structure of T and ω_z (Grooms et al. 2010, Rajaei et al. 2017) around the Taylor column and efficient heat transport. With further increase of $\widetilde{\mathcal{R}a}$, the vertical coherence of the convective Taylor columns is degraded and plumes only partially penetrate across the fluid layer with an even shorter vertical correlation length (Julien et al. 2012b, Nieves et al. 2014, Rajaei et al. 2017) (see **Figure 5*f*,*g***). For the highest investigated $\widetilde{\mathcal{R}a} \approx 20$ in the nonhydrostatic quasi-geostrophic model (Julien et al. 2012b) and for $\mathcal{P}r = 1$ (see **Figure 5*g***), one reaches a state of geostrophic turbulence in which heat transport is throttled by the interior rather than by thermal BLs. Experimental examples of geostrophic turbulence are shown in **Figure 5*h*** with $\widetilde{\mathcal{R}a} = 77$ and $\mathcal{R}o_c = 0.12$ and in **Figure 1*f*** with $\widetilde{\mathcal{R}a} = 27$ and $\mathcal{R}o_c = 0.024$. Finally, in certain circumstances DNS have shown that a large-scale vortex condensate forms from the geostrophic turbulence state (Julien et al. 2012b, Guervilly et al. 2014, Guervilly & Hughes 2017, Julien et al. 2018, Favier et al. 2019, de Wit et al. 2022). The regions of geostrophic turbulence and large-scale vortex condensate have sufficiently large $\widetilde{\mathcal{R}a}$ such that for experiments and DNS one may no longer be in the quasi-geostrophic regime but rather in the rotation-affected regime; large-scale vortex states have not been observed in experiments. Eventually, with increasing $\mathcal{R}a$ the flow enters the buoyancy-dominated regime, where the flow closely resembles turbulent nonrotating convection (Nieves et al. 2014, Cheng et al. 2015, Julien et al. 2016, Cheng et al. 2018) (see **Figure 1*b*,*i***). A detailed review of the quasi-geostrophic regime and its different regimes has been given by Kunnen (2021). Although the qualitative and semiquantitative features predicted from the quasi-geostrophic model agree fairly well with observations from experiments and DNS, significant details remain to be determined, including how Ekman pumping and non-quasi-geostrophic effects manifest in systems at finite $\mathcal{E}k$ and $\mathcal{R}o$. As a starting point, the solutions of the nonhydrostatic quasi-geostrophic equations exhibit for $\mathcal{P}r = 7$ transitions from cellular to convective Taylor columns state at $\widetilde{\mathcal{R}a} \approx 2$, transitions from convective Taylor columns to plumes at $\widetilde{\mathcal{R}a} \approx 6$, and plumes to geostrophic turbulence at $\widetilde{\mathcal{R}a} > 17$ (no transition is observed).

2.1.1. Columnar regime (for $\mathcal{P}r \gtrsim 3$). The columnar regime (**Figure 5*a–c***) is characterized by quasi-steady convective Taylor columns (Veronis 1959, Heard & Veronis 1971, Sakai 1997) that are built of vertically coherent plumes emitted synchronously from the hot and cold BLs. Each column consists of a hot (cold) central region with a cyclonic (anticyclonic) vortex core surrounded by a region of opposite temperature contrast and oppositely signed vorticity (Sprague et al. 2006; Grooms et al. 2010; Julien et al. 2012b; King et al. 2012; Rajaei et al. 2016, 2017). The convective Taylor columns are nonuniformly distributed horizontally and the vortices undergo complex interactions including vortex mergers (Zhong et al. 1993, Noto et al. 2019), a flux of vortices away from the lateral boundary (Noto et al. 2019, Ding et al. 2021) attributed to centrifugal effects, and a diffusive-like motion of individual vortices in the overall vortex array (Chong et al. 2020, Ding et al. 2021). In this region, the shielding of the convective Taylor columns reduces vortex interactions and stabilizes the vortex array (Grooms et al. 2010, Rajaei et al. 2017). For experimentally and computationally accessible $\mathcal{E}k > 10^{-8}$, the effects of Ekman pumping are large (Stellmach et al. 2014, Julien et al. 2016, Plumley et al. 2016) and lead to a very rapid increase in $\mathcal{N}u$ in this regime for $\mathcal{P}r \approx 7$ compared to the expected asymptotic linear dependence, $\mathcal{N}u - 1 = a\epsilon + \mathcal{O}(\epsilon^2)$, with $a \approx 2$ (Bassom & Zhang 1994, Dawes 2001). **Figure 6*a*** shows $\mathcal{N}u - 1$ versus ϵ (reflecting $\mathcal{N}u = 1$ at $\widetilde{\mathcal{R}a} = 1$) for a variety of data (after figure 5 of Stellmach et al. 2014). The lowest values of $\widetilde{\mathcal{R}a}$ are consistent with the weakly nonlinear solution with $a \approx 2$, but the $\mathcal{O}(\epsilon^2)$ term is 20 times larger than the nonhydrostatic quasi-geostrophic results, indicating that Ekman pumping is felt even very close to onset. The power law relationship for the data in the convective Taylor columns regime is $\mathcal{N}u - 1 \sim (\widetilde{\mathcal{R}a} - 1)^{5/3}$, as compared to $\mathcal{N}u \sim \widetilde{\mathcal{R}a}^3$ (Stellmach et al. 2014); the effective scaling exponent is very sensitive to subtracting 1 unless $\mathcal{N}u \gg 1$ and $\widetilde{\mathcal{R}a} \gg 1$. One also notes from **Figure 6*a*** that the convective Taylor columns persist to higher $\widetilde{\mathcal{R}a}$ for smaller $\mathcal{E}k$. For $\mathcal{P}r = 1$, Ekman pumping has a similar effect on the slope of $\mathcal{N}u$ near onset, although the convective Taylor columns regime is not observed (Julien et al. 2012b). Other characterizations of the convective Taylor columns state include a rapid decrease in the mean temperature gradient (**Figure 6*b***) and increasing normalized root-mean-square (rms) averages $\omega_{z_{\mathrm{rms}}}$ (**Figure 6*c***) and T_{rms} (**Figure 6*e***) for the nonhydrostatic quasi-geostrophic model. Available experimental data (Vorobieff & Ecke 2002, Shi et al. 2020) agree with the increase of $(\omega_{z_{\mathrm{rms}}}/\Omega)\mathcal{E}k^{-1/3}$ in this regime. Although there is no experimental data in this regime for T_{rms}, DNS data (Aguirre Guzmán et al. 2022), when normalized as $(T_{\mathrm{rms}}/\Delta)\mathcal{E}k^{-1/3}$, show a similar increasing trend for small $\widetilde{\mathcal{R}a}$ with a similar magnitude.

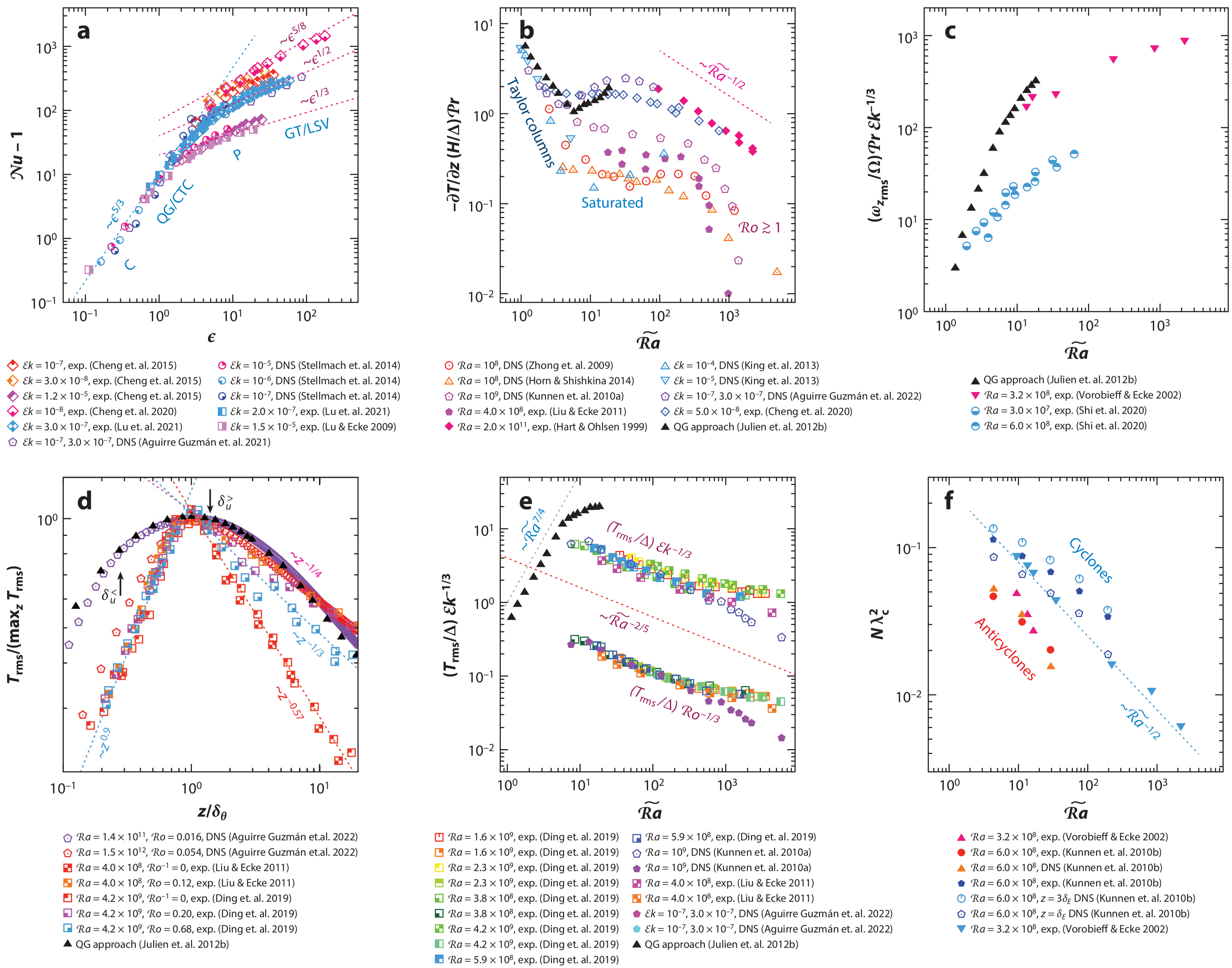

(Caption appears on following page)

Figure 6 (*Figure appears on preceding page*)

(*a*) $\mathcal{N}u - 1$ versus $\epsilon \equiv \widetilde{\mathcal{R}a} - 1$, with $\widetilde{\mathcal{R}a} \equiv \mathcal{R}a/\mathcal{R}a_c - 1$, for the nonhydrostatic quasi-geostrophic regions and approximate scalings. (*b*) Normalized vertical temperature gradient $-\partial T/\partial z\,(H/\Delta)\mathcal{P}r$ versus $\widetilde{\mathcal{R}a}$ for $4.4 \leq \mathcal{P}r \leq 8.8$. Smaller $\mathcal{R}a$ values have a smaller mean gradient and a wider saturation region. (*c*) Normalized rms of the vertical vorticity component $(\omega_{z_{\rm rms}}/\Omega)\,\mathcal{P}r\,\mathcal{E}k^{-1/3}$ versus $\widetilde{\mathcal{R}a}$. (*d*) rms of the temperature normalized by its maximum value $T_{\rm rms}/(\max_z T_{\rm rms})$ versus z/δ_θ, the distance from the plate normalized by the thermal BL thickness. Arrows indicate the approximate locations of the normalized thicknesses of the kinetic BL δ_u/δ_θ for the nonhydrostatic quasi-geostrophic ($\delta_u^<$) and power law ($\delta_u^>$) scaling regions for larger $\widetilde{\mathcal{R}a}$ (Aguirre Guzmán et al. 2021). (*e*) rms of the temperature normalized with Δ, the temperature difference between the plates, $(T_{\rm rms}/\Delta)\,\mathcal{E}k^{-1/3}$ [or $(T_{\rm rms}/\Delta)\,\mathcal{R}o^{-1/3}$] versus $\widetilde{\mathcal{R}a}$. (*f*) Vortex densities $\lambda_c^2 N_+$ and $\lambda_c^2 N_-$ versus $\widetilde{\mathcal{R}a}$: cyclonic (*blue*) and anticyclonic (*red*). For all panels, the Prandtl number is $\mathcal{P}r \approx 7$. Abbreviations: BL, boundary layer; C, cellular; CTC, convective Taylor columns; DNS, direct numerical simulations; exp., experiment; GT, geostrophic turbulence; LSV, large-scale vortices; P, plumes; QG, quasi-geostrophy; rms, root-mean-square.

2.1.2. Plume regime. The convective Taylor columns lose vertical coherence in the plume regime for $\mathcal{P}r \gtrsim 3$ (**Figure 5*f***) so that individual vortical structures terminate in the interior. In losing their coherence (King & Aurnou 2012), the plumes become increasingly desynchronized across the layer at larger $\widetilde{\mathcal{R}a}$ (Sprague et al. 2006, Julien et al. 2012b, King & Aurnou 2012, Rajaei et al. 2017). Nieves et al. (2014) and Cheng et al. (2020) suggested that a transition from columnar convection to a plume regime for large $\mathcal{P}r$ ($\mathcal{P}r \approx 7$) takes place at about $\widetilde{\mathcal{R}a} \approx 6$. This identification is consistent with DNS and experiments for $10^{-8} \lesssim \mathcal{E}k \lesssim 10^{-4}$ in terms of the following features: a change in slope of $\mathcal{N}u$ versus $\widetilde{\mathcal{R}a}$, a saturation of $\partial T/\partial z$, a reversal in the slope of $T_{\rm rms}$ (see Section 2.1.3), and a trend toward equalization of cyclonic and anticyclonic vortex density, as illustrated in **Figure 6*a*,*b*,*e***, and ***f***, respectively.

2.1.3. Geostrophic turbulence. The nonhydrostatic quasi-geostrophic model (Julien et al. 2012b) predicts that at $\mathcal{R}a \approx 5\mathcal{R}a_c$ (for $\mathcal{P}r \lesssim 3$), there is a transition to geostrophic turbulence where the geostrophic balance is maintained with the interior of the flow, as well as in the BL. In this regime, the vortical structures are very short and attached to the BLs, whereas the bulk flow is well mixed laterally and turbulent. Owing to geostrophic balance, the flow structures maintain a degree of vertical alignment (**Figure 1*f***) and an interior control of heat transport, as opposed to a BL-controlled process. The boundary separating plumes and geostrophic turbulence is more complex than the transition from convective Taylor columns to plumes (Cheng et al. 2020). For $\mathcal{P}r = 7$, geostrophic turbulence was not found in the nonhydrostatic quasi-geostrophic simulations. In **Figure 6*b***. the structure of the finite mean temperature gradient shows a saturated region in the range $10 \lesssim \widetilde{\mathcal{R}a} \lesssim 300$ corresponding to $10^8 \leq \mathcal{R}a \leq 10^9$, which decreases in range as $\mathcal{R}a$ increases or $\mathcal{E}k$ decreases (the $\mathcal{P}r$ factor multiplying $-\partial T/\partial z$ yields a better collapse of the data, with lower saturated mean gradient increasing with increasing $\mathcal{R}a$). The rapid decrease in slope for $\widetilde{\mathcal{R}a} \approx 300$ corresponds to $\mathcal{R}o \approx 1$. For the largest $10^{11} \lesssim \mathcal{R}a \lesssim 10^{12}$, there is a $\widetilde{\mathcal{R}a}^{-1/2}$ scaling over about 1.5 decades in $\widetilde{\mathcal{R}a}$ and a maximum at the slightly smaller $\widetilde{\mathcal{R}a} \approx 50$ [a shallower slope was fit (Cheng et al. 2020) to a subsection of the data close to the maximum with an effective slope of -0.21, rather than the $-1/2$ identified here, which is consistent with Hart & Ohlsen (1999)]. For this $\mathcal{R}a$ range, $\widetilde{\mathcal{R}a}$ is greater than 5,000 for $\mathcal{R}o \approx 1$. The nature of the saturation, the maximum, and the power law decrease are not fully understood; perhaps geostrophic turbulence modified by ageostrophic contributions exists for the lower $\widetilde{\mathcal{R}a}$ range of these observations, although the $\mathcal{N}u$ scaling is not consistent in this range with the nonhydrostatic quasi-geostrophic prediction of $\widetilde{\mathcal{R}a}^{3/2}$ (**Figure 6*a***). There is a striking difference in the trends of $T_{\rm rms}$ evaluated at its maximum value (with respect to z) versus $\widetilde{\mathcal{R}a}$ (**Figure 6*e***). The nonhydrostatic quasi-geostrophic model suggests normalizing $T_{\rm rms}$ with $\mathcal{E}k^{-1/3}$, and the experimental results are similar in magnitude when normalized in this manner, although the trends with $\widetilde{\mathcal{R}a}$ are the opposite. DNS data (Aguirre Guzmán et al. 2022) for $5 \times 10^9 \leq \mathcal{R}a \leq 1.5 \times 10^{12}$ span the range $1.3 < \widetilde{\mathcal{R}a} < 80$ and bridge the gap between nonhydrostatic quasi-geostrophic predictions and experiment. The lower $\widetilde{\mathcal{R}a}$ values agree well with the nonhydrostatic quasi-geostrophic results, whereas the $\widetilde{\mathcal{R}a} = 80$ value is significantly (by about a factor of 3) larger than the corresponding experimental data. For nonhydrostatic quasi-geostrophic results, one has $(T_{\rm rms}/\Delta)\mathcal{E}k^{-1/3} \sim \widetilde{\mathcal{R}a}^{7/4}$ for $\widetilde{\mathcal{R}a} \leq 7$ approaching a constant for higher values, whereas the data from experiments with $3 \times 10^8 \lesssim \mathcal{R}a \lesssim 5 \times 10^9$ show scaling to be approximately $\sim\widetilde{\mathcal{R}a}^{-2/5}$ up to about $\widetilde{\mathcal{R}a} \approx 500$. A scaling that better collapses the DNS and experimental data is $(T_{\rm rms}/\Delta)\mathcal{R}o^{-1/3}$, implying that there is a remnant $\mathcal{R}a$ (and $\mathcal{E}k$) dependence that accounts for the magnitude shift. The maximum of $T_{\rm rms}$ at $\widetilde{\mathcal{R}a} \approx 7$ indicates that the scaling for larger $\widetilde{\mathcal{R}a} \leq 7$ results from the plume transition and is not affected by the crossover to geostrophic turbulence. A final feature of $T_{\rm rms}$, for $\delta_u \geq \delta_\theta$, is that its variation with z takes on a universal shape of a maximum value at the thermal BL thickness with different effective power law scalings inside and outside that layer (Ding et al. 2019, figure 6*d*). For $z/\delta_\theta < 1$, we have $T_{\rm rms}(z) \sim z^{0.9}$, independent of rotation, whereas outside the BL one has an $\mathcal{R}o$-dependent effective scaling going from $\sim z^{-0.6}$ for the nonrotating case to $\sim z^{-0.25}$, where the effective scaling exponent is approximately constant for $\mathcal{R}o \lesssim 0.5$ (Ding et al. 2019, figure 2*b*). For these data, one has $\delta_\theta \approx \delta_u$, indicating that they are not in the quasi-geostrophic limit. The nonhydrostatic quasi-geostrophic results are quite different for $\delta_\theta \gg \delta_u$, with similar magnitude but without an effective power law scaling for $z/\delta_\theta > 1$, but with much larger fluctuations and again no power law scaling for $z/\delta_\theta < 1$, where presumably Ekman pumping effects play a leading role (Stellmach et al. 2014, Julien et al. 2016).

Geostrophic turbulence can support an inverse energy transfer process that results in the formation of large-scale vorticity. Although similar in outcome (i.e., a large-scale vortex condensate), the energy transfer is a direct one from small scales to large scales via 3D modes and thus is different from a purely 2D inverse energy cascade (Boffetta & Ecke 2012). These flows have been seen in DNS (Julien et al. 2012b; Favier et al. 2014; Guervilly et al. 2014; Rubio et al. 2014; Stellmach et al. 2014; Kunnen et al. 2016; Kunnen 2021) for a variety of Γ (Guervilly & Hughes 2017, Julien et al. 2018), for different $\mathcal{P}r$ (Maffei et al. 2021), and for free-slip and no-slip BCs at the plates (Aguirre Guzmán et al. 2020). Such large-scale vortices, however, have only been observed in simulations with periodic BCs in horizontal directions, and the formation of these vortices depends on Γ (Guervilly & Hughes 2017, Julien et al. 2018) and on initial conditions (Favier et al. 2019). Whether these large-scale vortex states persist in real experiments with sidewalls and with significant $\widetilde{\mathcal{R}a} \gg 1$, where other physics may dominate, remains an open question.

2.1.4. Boundary zonal flow and transitions to the rotation-affected regime. RRBC turbulence in a laterally confined geometry is also characterized by the presence of a BZF located close to the container sidewall (de Wit et al. 2020; Zhang et al. 2020, 2021; Wedi et al. 2021), which can be understood as the remnant of wall modes (Favier & Knobloch 2020, Ecke et al. 2022). The BZF has been directly and indirectly observed from the onset of bulk convection up to the transition to buoyancy-dominated flows at $\mathcal{R}o \approx 2$. It is especially influential in systems with $\Gamma \leq 1$, which have been utilized for experimental purposes to reach extremes of system parameters. The fluid motion within the BZF is cyclonic (prograde) whereas the temperature pattern drifts anticyclonically (retrograde). Within the BZF the vertical heat flux can be $\gtrsim$60% larger than the average $\mathcal{N}u$, making the BZF particularly significant (Zhang et al. 2021). DNS by Ecke et al. (2022) for a fixed $\mathcal{E}k = 10^{-6}$ and varying $\mathcal{R}a$ showed a direct connection between pure wall modes, which occur prior to bulk convection, and the BZF that coexists with turbulent convective flow in the bulk. The impact of the BZF on flows in realistic physical geometries is only recently beginning to be appreciated, and its existence may offer explanations for several observations, such as the varying slope of $\mathcal{N}u$ versus $\mathcal{R}a$ near onset [DNS by Lu et al. (2021)] and the attribution of a deficit of vortex density at the walls to centrifugal (Noto et al. 2019) or proximity (Weiss & Ahlers 2011b) effects.

2.2. Rotation-Affected and Buoyancy-Dominated Turbulence

Here we detail the transition from the rotation-dominated regime to the rotation-affected regime and the transition to buoyancy-dominated turbulence. The characteristics of these transitions are a change in slope of $d\mathcal{N}u/d\mathcal{R}a$ and the parameters for which $\mathcal{N}u \rightarrow \mathcal{N}u_0$. For fixed $\mathcal{P}r$, one takes the quantity $\mathcal{E}k^{\alpha_0}\mathcal{R}a$ as the combined transition parameter, where α_0 is chosen to provide the best collapse of the data—one typically uses $\mathcal{N}u$ as the indicator of the transitions. Theory and experiment provide several choices in the range $4/3 \leq \alpha_0 \leq 2$, with the limits corresponding to $\widetilde{\mathcal{R}a} \sim \mathcal{E}k^{4/3}\mathcal{R}a$ and $\mathcal{R}o^2 \sim \mathcal{E}k^2\mathcal{R}a$. These transitions are discussed in detail by Kunnen (2021).

2.2.1. Rotation-affected regime. As seen in **Figure 1*b***, $\mathcal{N}u$ at constant $\mathcal{E}k$ increases rapidly with $\mathcal{R}a$ from its unity value at onset toward an asymptotic value corresponding to its nonrotating value $\mathcal{N}u_0$. For $\mathcal{R}a \lesssim 10^{10}$ and $\mathcal{P}r \gtrsim 1$, $\mathcal{N}u$ exceeds $\mathcal{N}u_0$ owing to Ekman pumping, which gives a concrete transition point, $\mathcal{N}u(\mathcal{R}a_t, \mathcal{E}k) = \mathcal{N}u_0$. For larger $\mathcal{R}a$ and smaller $\mathcal{E}k$, we have $\mathcal{N}u \leq \mathcal{N}u_0$, so that the transition value is given by a sharp decrease in the slope $\mathrm{d}\mathcal{N}u/\mathrm{d}\mathcal{R}a$. This rotation-affected regime, which separates the rotation-dominated and buoyancy-dominated regimes, is characterized by the presence of vortical thermal plume emission from the BLs and the absence of an LSC (Vorobieff & Ecke 2002; Kunnen et al. 2008; Weiss & Ahlers 2011a,b,c). The heat transport can be more efficient than it is for nonrotating convection owing to Ekman pumping (e.g., Rossby 1969; Zhong et al. 1993; Julien et al. 1996; Liu & Ecke 1997, 2009; Zhong et al. 2009; Stevens et al. 2010a; King et al. 2009) for $\mathcal{P}r \gtrsim 1$ and, if $\mathcal{R}a$ is sufficiently small, $\mathcal{R}a \lesssim 10^{10}$. King et al. (2009) suggested that the transition value into the rotation-affected regime for $\mathcal{P}r \approx 7$ was determined by an approximate equivalence of thermal and Ekman BL thicknesses [i.e., $\delta_\theta \approx (2\mathcal{N}u)^{-1} \approx \delta_E$ with an empirical transition $\mathcal{R}a_t \approx 1.4\mathcal{E}k^{-7/4}$, which was later modified to $\mathcal{R}a_t \approx 10\mathcal{E}k^{-3/2}$ (see King et al. 2012, 2013; King & Aurnou 2013)]. Liu & Ecke (2009) suggested $\mathcal{R}o = 0.1$, corresponding to $\mathcal{R}a_t \approx 0.06\mathcal{E}k^{-2}$. The nonhydrostatic quasi-geostrophic approach predicts a breakdown of geostrophic balance at $\mathcal{R}a_t \sim \mathcal{P}r^{3/5}\mathcal{E}k^{-8/5}$. Measurements for $\mathcal{P}r \approx 0.7$ (Ecke & Niemela 2014) gave $\mathcal{R}a_t \approx 0.25\mathcal{E}k^{-1.8}$ and recast the results of Liu & Ecke (2009) as $\mathcal{R}a_t \approx 1.3\mathcal{E}k^{-1.65}$, in close agreement with results of King et al. (2009). Recent results (Lu et al. 2021) for $\mathcal{P}r \approx 4$ indicated $\mathcal{R}a_t \approx 0.2\mathcal{E}k^{1.7}$, while Wedi et al. (2021) found $\mathcal{R}a_t \approx 0.8\mathcal{E}k^{-2}$. Finally, Cheng et al. (2018, 2020) identified a transition to a so-called unbalanced BL regime, which is associated with a breakdown of quasi-geostrophy in the thermal BL, while the quasi-geostrophic condition is maintained in the interior at $\mathcal{R}o_t \approx 0.06$. How exactly factors such as aspect ratio Γ, $\mathcal{P}r$, or the contributions of a BZF in finite containers affect this transition has yet to be worked out in detail. Nevertheless, the rotation-affected regime is rich with interesting crossovers from the quasi-geostrophic to buoyancy-dominated flow.

2.2.2. Buoyancy-dominated regime. The final regime is the rotation-unaffected buoyancy-dominated regime. Extensive measurements by Weiss & Ahlers (2011a,b) and Weiss et al. (2016) have indicated that the transition where $\mathcal{N}u \rightarrow \mathcal{N}u_0$ occurs for $\mathcal{R}o_{t2} \approx 1.3\,\mathcal{P}r^{0.41}$ is within the range $3 \lesssim \mathcal{P}r \lesssim 35$ and $10^9 \lesssim \mathcal{R}a \lesssim 10^{12}$. Lu et al. (2021) suggested for this transition $\mathcal{R}a_{t2} \approx 3.4\mathcal{E}k^{-1.7}$ (water), whereas Wedi et al. (2021) indicated $\mathcal{R}o_{t2} = 1.3$ for $\mathcal{P}r \approx 0.8$. This transition was also found empirically to vary with Γ as $\mathcal{R}o^{-1} = c_1\Gamma^{-1}(1 + c_2\Gamma^{-1})$, with $c_1 \approx 0.38$ and $c_2 \approx 0.06$ (Weiss & Ahlers 2011a,b). It can be argued that at this transition the buoyant and the Coriolis timescales become similar, $\tau_{\mathrm{ff}} \sim \tau_\Omega$ (i.e., $\mathcal{R}o \sim 1$). In the buoyancy-dominated regime, the flows and the scalings are similar to those in nonrotating turbulent RBC (Ahlers et al. 2009b) because the effect of the Coriolis forces becomes negligible.

2.2.3. From large-scale circulation to boundary zonal flow. When rotation is slow, the turbulent RBC flow looks similar to the nonrotating case. In nonrotating turbulent RBC in containers of $\Gamma \sim 1$, an LSC develops (Ahlers et al. 2009b). There is a vertical central cross section (an LSC plane), in which a large LSC roll fills the core part with secondary rolls in the corners. The LSC can undergo twisting, sloshing, and other motions (see, e.g., Cioni et al. 1997; Funfschilling & Ahlers 2004; Xi et al. 2004, 2006; Wagner et al. 2012). Since the LSC is always tilted, in another vertical cross section orthogonal to the LSC plane, the flow typically looks like a four-roll structure, with an inflow in the central horizontal cross section (Shishkina et al. 2013, 2014). Under slow rotation, at mid-height, the flow toward the center is affected by the Coriolis force in such a way that a cyclonic (prograde) fluid motion is induced there (Kunnen et al. 2011). Near the plates, however, the LSC flow toward the sidewall under the action of the Coriolis force leads to an anticyclonic (retrograde) fluid motion there (see Zhang et al. 2021, figure 2). Near the centerline and close to the plates, the flow remains anticyclonic for all Ω. As rotation increases, the mean flow structure tends to be homogeneous in the vertical direction (according to the Taylor–Proudman constraint), which results in the following: The region of the anticyclonic motion grows from the plates toward the bulk and finally occupies the core part of the domain, whereas the region of cyclonic motion, which forms the BZF, is pushed toward the sidewall and shrinks with increasing Ω ($\mathcal{R}o^{-1}$). Thus, at a certain constant $\mathcal{R}o$ of order one, a breakdown of the LSC happens (Vorobieff & Ecke 2002; Kunnen et al. 2008; Weiss & Ahlers 2011a,b,c) and a BZF becomes the most prominent system-spanning global structure (de Wit et al. 2020; Zhang et al. 2020, 2021; Ecke et al. 2022).

2.3. Other Characteristics of RRBC Flows

There are many other characteristics of RRBC flows that have been either computed from DNS or measured directly in physical experiment. Our review has selected what we view as the central quantities that represent the problem. Here we discuss several others of interest.

2.3.1. Toroidal and poloidal energies. The change of flow structures is also tracked in the evolution of the toroidal (e_{t}) and poloidal (e_{p}) kinetic energies (Horn & Shishkina 2015). For moderate $\mathcal{R}a$, e_{t} is less than e_{p} if buoyancy dominates and e_{p} gradually decreases with stronger rotation. With increasing $\mathcal{R}o^{-1}$, e_{t} increases in the rotation-affected regime until it achieves $e_{\mathrm{t}} = e_{\mathrm{p}}$; this location can be interpreted as the beginning of rotation dominance where e_{t} is greater than e_{p}.

2.3.2. Statistical moments of temperature, velocity, and vorticity. The statistical moments of the convective fields (T, $\mathbf{u}$, and ω_z) are important indicators of the physics of RRBC and elucidate its similarities and differences with nonrotating RBC (Julien et al. 1996, 2012b). In experiments, single point probes of T are utilized (Liu & Ecke 1997, 2011; Hart & Ohlsen 1999; Hart et al. 2002; Ding et al. 2019) and the dependence on the distance to the plate z can be determined. Similar measurements can be performed using DNS (Kunnen et al. 2010a, Aguirre Guzmán et al. 2022). There is a maximum of T_{rms} at $z = \delta_\theta$ and larger fluctuations at $z = \delta_\theta$, as well as at the mid-plane $z = H/2$, compared to the nonrotating case. Both the skewness (sign preference) and kurtosis (Gaussianity measure) of T are smaller than they are for nonrotating RBC at a particular z, and they are small near the thermal BL and increase with z, reaching a max value at about $10\delta_\theta$ (Liu & Ecke 2011, Ding et al. 2019); the skewness is approximately 0 at the mid-plane owing to symmetry [cf. Aguirre Guzmán et al. (2022) for the Taylor columns state]. In DNS (Aguirre Guzmán et al. 2022), it is possible to evaluate statistics and average over horizontal planes, which are very difficult to obtain in experiments. The DNS show that the skewness is preferentially negative for $\delta_u < \delta_\theta$ but becomes positive for the reverse. This is consistent with single point measurements (Liu & Ecke 2011, Ding et al. 2019) inside the thermal BL for the conditions $\delta_\theta \approx \delta_u$. The kurtosis of T is uniformly greater than 3, indicating stretched exponential probability density functions (PDFs). The skewness of horizontal velocity and ω_z are $\approx$0 (Vorobieff & Ecke 2002, Kunnen et al. 2010b, Aguirre Guzmán et al. 2022) at the mid-plane, with exponential tails rather than the Gaussian PDFs for nonrotating RBC. Near the plates there is skewness toward cyclonic vorticity and positive u_z with strong non-Gaussianity. This is consistent with the picture in **Figure 2** regarding cyclonic vorticity generation and Ekman pumping–induced upward flow, $u_z > 0$. The nature of fluctuations near the plates is an important subject that needs additional study to further elucidate the interactions of the thermal and kinetic BLs in the presence of Ekman pumping (Stellmach et al. 2014, Julien et al. 2016, Plumley et al. 2016).

3. HEAT TRANSPORT IN RRBC

The global measure of RRBC is the convective enhancement of heat transport $\mathcal{N}u$. There are clear scaling relationships in the limits of rotation-dominated and buoyancy-dominated regimes, as discussed above. In between, the situation is less clear cut. We assume for the sake of comparison that there is power law scaling in the range of convective Taylor columns/plumes $2 \lesssim \widetilde{\mathcal{R}a} \lesssim 10$ (see **Figure 6*a***), although Ekman pumping contributes significantly here. There are no theoretical predictions for this region.

3.1. Measurements and Simulations of Heat Transport in RRBC

Experimental measurements of $\mathcal{N}u$ require fine system control and precision in heat flow [e.g., accurately measuring the heat flow through the fluid as opposed to measuring through sidewalls, evaluating non-OB effects, introducing proper heat shielding, and measuring control variables such as temperature difference and heat current (Ahlers et al. 2009b)]. DNS measures complement experiments by allowing access to the full fields of temperature and velocity but require very fine grids and long computing times to obtain good statistical averages. To properly interpret $\mathcal{N}u$ one must be aware of wall modes that contribute at the onset of bulk convection and continue to influence total $\mathcal{N}u$ through the coexisting BZF. This contribution can be fractionally large for convection in small Γ (e.g., Zhang et al. 2020, de Wit et al. 2020, Ecke et al. 2022). We now describe the evolution of $\mathcal{N}u$ in different regimes, starting from onset $\widetilde{\mathcal{R}a} = 1$ and ending with $\mathcal{R}o \gg 1$ (i.e., the nonrotating limit).

After a small region of weakly nonlinear growth for $\epsilon \lesssim 1$, $\mathcal{N}u$ rises steeply owing to Ekman pumping (Stellmach et al. 2014, Julien et al. 2016, Plumley et al. 2016) for $\mathcal{P}r = 1$ and $\mathcal{P}r = 7$, as $\mathcal{N}u - 1$ scales as $\epsilon^{5/3}$—or, without the subtracted value of 1, as $\mathcal{N}u \sim \widetilde{\mathcal{R}a}^3$ [earlier analysis and explanations did not include the important Ekman pumping effect (Boubnov & Golitsyn 1995; Canuto & Dubovikov 1998; King et al. 2009, 2012; Ecke 2015)]. The initial steepening increases with decreasing $\mathcal{E}k$ (Cheng et al. 2015), but the modified nonhydrostatic quasi-geostrophic model suggests that Ekman pumping reaches its maximum at $\widetilde{\mathcal{R}a} \approx 3$ for $\mathcal{E}k = 10^{-7}$ (see Plumley et al. 2016, figures 4 and 14), with factors of 2.5 and 10 of higher $\mathcal{N}u$ compared to the nonhydrostatic quasi-geostrophic prediction for $\mathcal{P}r = 1$ and $\mathcal{P}r = 7$, respectively. The latter is in the same range as the data presented in **Figure 6*a***, where the maximum amplification factor is about 6. The region where the maximum enhancement occurs is within the convective Taylor columns or plume regime, depending on $\mathcal{P}r$. Following the rapid increase, the effective scaling of $\mathcal{N}u$ with $\widetilde{\mathcal{R}a}$

continuously decreases toward an asymptotic buoyancy-dominated effective scaling of $\mathcal{N}u \sim \mathcal{R}a^{0.3}$ (Cheng et al. 2020), although less slowly for smaller $\mathcal{E}k$ (see **Figure 6*a***). The same trend is seen in figure 3 of Lu et al. (2021), with the observation that there is an apparent wall mode/BZF contribution $\Delta\mathcal{N}u \approx 10$, as per Ecke et al. (2022). How much of $\mathcal{N}u$ in this region is contributed by the BZF is a matter of current research. In contrast, for $\mathcal{E}k \gtrsim 10^{-6}$, $\mathcal{N}u$ undergoes a rapid transition to BL-controlled convection with Ekman pumping enhancement with approximate $\mathcal{R}a^{1/3}$ scaling for $10 \lesssim \widetilde{\mathcal{R}a} \lesssim 100$. For smaller $\mathcal{E}k$, the transition is to $\sim\widetilde{\mathcal{R}a}^{1/2}$ and $\sim\widetilde{\mathcal{R}a}^{5/8}$ for $\mathcal{E}k \approx 10^{-7}$ and 10^{-8}, respectively. This may indicate a transition toward geostrophic turbulence with an expected Ekman pumping–adjusted dependence of $\mathcal{N}u \approx 0.04(1 + 5.97\mathcal{E}k^{1/8})\mathcal{P}r^{-1/2}\mathcal{E}k^2\mathcal{R}a^{3/2}$ (Julien et al. 2012b, Plumley et al. 2017) for smaller $\mathcal{E}k$.

As $\mathcal{R}a$ increases further, one arrives in a region where $\mathcal{R}o$ is no longer small. The condition $\mathcal{R}o \approx 1$ then yields an upper bound on the rotation-affected regime of $\widetilde{\mathcal{R}a}_{\rm t} \approx (\mathcal{P}r/A)\mathcal{E}k^{-2/3}$, where we have $A = \mathcal{R}a_{\rm c}\mathcal{E}k^{4/3}$. For $\mathcal{P}r = 7$, one has $2{,}000 \lesssim \widetilde{\mathcal{R}a}_{\rm t} \lesssim 2 \times 10^5$ for $10^{-8} \lesssim \mathcal{E}k \lesssim 10^{-5}$. Based on the earlier quasi-geostrophic analysis, one can estimate that the transition from the quasi-geostrophic to rotation-affected regime is in the range $100 \lesssim \widetilde{\mathcal{R}a}_{\rm t} \lesssim 2 \times 10^5$, depending on $\mathcal{E}k$. Within this range, different scalings and data-collapse strategies have been proposed. The effective scaling exponents are very sensitive to the $\mathcal{R}a$ and $\mathcal{E}k$ ranges where the fits are made, as this is exactly the region that connects very different scaling regimes of the dominance of rotation and of buoyancy. In the rotation-affected regime, for $\mathcal{P}r \gtrsim 1$ and not too large $\mathcal{R}a \lesssim 10^{10}$, $\mathcal{N}u$ is larger than it is for the nonrotating case ($\mathcal{N}u_0$), owing to the positive Ekman pumping effect noted above and the relatively low value of $\mathcal{N}u_0$ (Stevens et al. 2010b, 2013; Horn & Shishkina 2014). Based on DNS for $4.38 \leq \mathcal{P}r \leq 100$ and $10^7 \leq \mathcal{R}a \leq 10^9$, Yang et al. (2020) obtained the optimal $\mathcal{R}o_{\rm o}^{-1} \approx 0.12\,\mathcal{P}r^{1/2}\mathcal{R}a^{1/6}$, at which, for fixed $\mathcal{R}a$ and varying $\mathcal{R}o$, the maximal $\mathcal{N}u/\mathcal{N}u_0$ was observed. The optimal heat transport relative to $\mathcal{N}u_0$ was obtained for this range of $\mathcal{R}a$ when the thicknesses of the thermal BL (estimated as $\sim\mathcal{R}a^{-1/3}$) and the viscous Ekman BL ($\sim \mathcal{E}k^{1/2}$) are similar. For comparison with data in **Figure 6*a***, one also has the result for optimal $\mathcal{N}u$ at $\widetilde{\mathcal{R}a} \approx 3\mathcal{E}k^{-1/6}$, which yields something in the range of $10 \lesssim \widetilde{\mathcal{R}a} \lesssim 20$ for $8 \times 10^{-6} \lesssim \mathcal{E}k \lesssim 2 \times 10^{-4}$. As one can see from **Figure 6*a***, this brackets a quite narrow range in the nonhydrostatic quasi-geostrophic diagram and severely limits access to quasi-geostrophic states.

In the buoyancy-dominated regime, the asymptotic scalings are independent of $\mathcal{E}k$, as in nonrotating turbulent RBC (Ahlers et al. 2009b). For measurements in experiments used for RRBC, the nonrotating effective scalings $\mathcal{N}u_0 \sim \mathcal{R}a^{\gamma}$ with $\gamma \approx 0.308$ (Cheng et al. 2020), $\gamma \approx 0.317$ (Lu et al. 2021), and $\gamma \approx 0.322$ (Cheng et al. 2015) for $\mathcal{R}a \lesssim 10^{14}$ are consistent with nonrotating measurements in the same ranges; smaller effective exponents $\gamma \approx 0.29$ are seen at lower $\mathcal{R}a$ (Rossby 1969, Zhong et al. 1993, Liu & Ecke 1997, King et al. 2009, Cheng et al. 2015). With rotation of these devices, $\mathcal{N}u$ approaches $\mathcal{N}u_0$ in the limit $\mathcal{R}o^{-1} \to 0$.

The transitions between different regimes may depend on Γ. For example, a rotation-affected to buoyancy-dominated transition scales empirically as $\mathcal{R}o^{-1} = c_1\Gamma^{-1}(1 + c_2\Gamma^{-1})$ with $c_1 \approx 0.38$ and $c_2 \approx 0.06$ (Weiss & Ahlers 2011a,b). Although Γ is very important in nonrotating convection (Shishkina 2021, Ahlers et al. 2022), the argument has been made (e.g., Liu & Ecke 1997, Julien et al. 2012a, Kunnen 2021) that from the nonhydrostatic quasi-geostrophic perspective, Γ should not play a large role provided the lateral horizontal scale ℓ/H is much less than $D/H = \Gamma$, which is well satisfied in most RRBC experiments given $\ell \sim \mathcal{E}k^{1/3}$. Thus, tall thin experiments have been constructed with $1/20 \leq \Gamma \leq 1/2$ (Cheng et al. 2018) (**Figure 3**). This assumption has been challenged by the unexpected robustness of wall mode/BZF states that contribute more strongly for small Γ (de Wit et al. 2020; Zhang et al. 2020, 2021; Ecke et al. 2022), approximately as $\sim\Gamma^{-1}$, and that centrifugal effects scale with H (Horn & Aurnou 2018). An example of the BZF contribution is that the increasing slope of $\mathcal{N}u$ with increasing Γ from Lu et al. (2021) is well explained by a decreasing wall mode/BZF contribution $\propto\Gamma^{-1}$. An important note here is that for any finite Γ, even for $\Gamma \gg 1$, numerical solutions for periodic BCs at the lateral boundaries of the computational domain are different from the solutions for experimental BCs. Although the difference vanishes in the limit $\Gamma \to \infty$, in realistic simulations with periodic BCs, Γ is relatively small, which causes significant differences in results compared to experiments or DNS with experimental BCs.

3.2. Hypothesis-Testing: Comparison of Measurements and Simulations

Let us now consider examples of heat transport data for RRBC in cylindrical containers with $\Gamma \approx 1/2$ using working gases He, N_2, or SF_6 for $0.7 \leq \mathcal{P}r \leq 0.9$ and water for $4 \leq \mathcal{P}r \leq 6$. In **Figure 7**, the data are plotted in two classical ways: at constant $\mathcal{R}a$ and varying $\mathcal{E}k$ (or $\mathcal{R}o$) (**Figure 7*a*,*c***) and at a constant $\mathcal{E}k$ and varying $\mathcal{R}a$ (**Figure 7*b*,*d***). In most models $\mathcal{N}u \sim \mathcal{R}a^{\gamma}$ is assumed with $\gamma = 1/3$ in the buoyancy-dominated regime, whereas the proposed values of ξ in $\mathcal{N}u \sim (\mathcal{R}a/\mathcal{R}a_c)^{\xi}$ in the rotation-dominated regime are different. For example, assuming that heat flux q is independent of H (or of ν and κ), one obtains $\xi = 3$ (or $\xi = 3/2$).

In **Figure 8** we tested different hypotheses using the data from **Figure 7** and plotted them as $\mathcal{N}u/\mathcal{R}a^{\gamma} \sim [\mathcal{E}k^{(4/3)\xi/(\xi-\gamma)}\mathcal{R}a]^s$, with $s = 0$ in the buoyancy-dominated regime and $s = \xi - \gamma$ in the rotation-dominated regime, for gases (**Figure 8*a*–*e***) and water (**Figure 8*f*–*j***); for $\xi = 1$ (**Figure 8*a*,*f***), $\xi = 3/2$ (**Figure 8*b*,*e*,*g*,*j***), $\xi = 2$ (**Figure 8*c*,*h***), and $\xi = 3$ (*d*,*i*); and for $\gamma = 1/3$ (**Figure 8*a*–*d*,*f*–*i***) and $\gamma = 1/2$ (**Figure 8*e*,*j***). The transition from the buoyancy-dominated to the rotation-dominated regimes then takes place at constant $\mathcal{E}k^{(4/3)\xi/(\xi-\gamma)}\mathcal{R}a$. It is remarkable that both combinations, $\gamma = 1/3$ and $\xi = 1$ and $\gamma = 1/2$ and $\xi = 3/2$, imply a transition at constant $\mathcal{E}k^2\mathcal{R}a$ (i.e., at constant $\mathcal{R}o$; see also Section 1.2.4). For the available data for gases one has $1 < \xi < 3/2$ (**Figure 8*a*,*b***), and $\xi = 3/2$ nicely represents the slope in the rotation-dominated regime for water (**Figure 8*g*,*j***). For different measurements and DNS, however, the rotation-affected and buoyancy-dominated data look quite different, being strongly overestimated with $\gamma = 1/2$ (**Figure 8*e*,*j***). Thus, a better way to represent the $\mathcal{N}u$ data in RRBC is needed, and in the next section we suggest such a description.

3.3. Scaling Theory for Heat Transport in Turbulent RRBC

Here we develop a unifying scaling approach for the transition from rotation-dominated to buoyancy-dominated regimes in turbulent RRBC. Summarizing different approaches to estimate heat transport scalings in these regimes, we identify two main ideas. First, in the rotation-dominated regime we have $\mathcal{N}u - 1 \sim (\mathcal{R}a/\mathcal{R}a_c)^{\xi}$, and in the buoyancy-dominated regime we have $\mathcal{N}u - 1 \sim \mathcal{R}a^{\gamma}$ for $\xi > 0$ and $\gamma > 0$. Second, there is a balance of the thicknesses of the viscous Ekman BL, $\delta_E/H \sim \mathcal{E}k^{1/2}$, which is thinner in the rotation-dominated regime, and of the thermal BL, $\delta_\theta/H \sim \mathcal{N}u^{-1}$, which is thinner in the buoyancy-dominated regime. Usually considered as independent, these ideas are, however, naturally connected because the change of the scaling regimes in RRBC is related to the change in the BL thickness balance. We thus combine these two ideas, leaving the exponents ξ and γ unspecified, and assume that in turbulent regimes $\mathcal{N}u$ is large (i.e., $\mathcal{N}u \gg 1$). These arguments give us the following relations, valid for the transition from rotation-dominated to buoyancy-dominated regimes:

$$\mathcal{N}u \sim \mathcal{R}a^{\gamma} \sim (\mathcal{E}k^{4/3}\mathcal{R}a)^{\xi} \quad \text{and} \quad \mathcal{N}u^{-1} \sim \delta_\theta/H \sim \delta_E/H \sim \mathcal{E}k^{1/2}. \qquad 10.$$

From Equation 10 we find the desired relations between the scaling exponents ξ and γ:

$$\xi = 3\gamma/(3 - 8\gamma) \quad \text{or, equivalently,} \quad \gamma = 3\xi/(3 + 8\xi). \qquad 11.$$

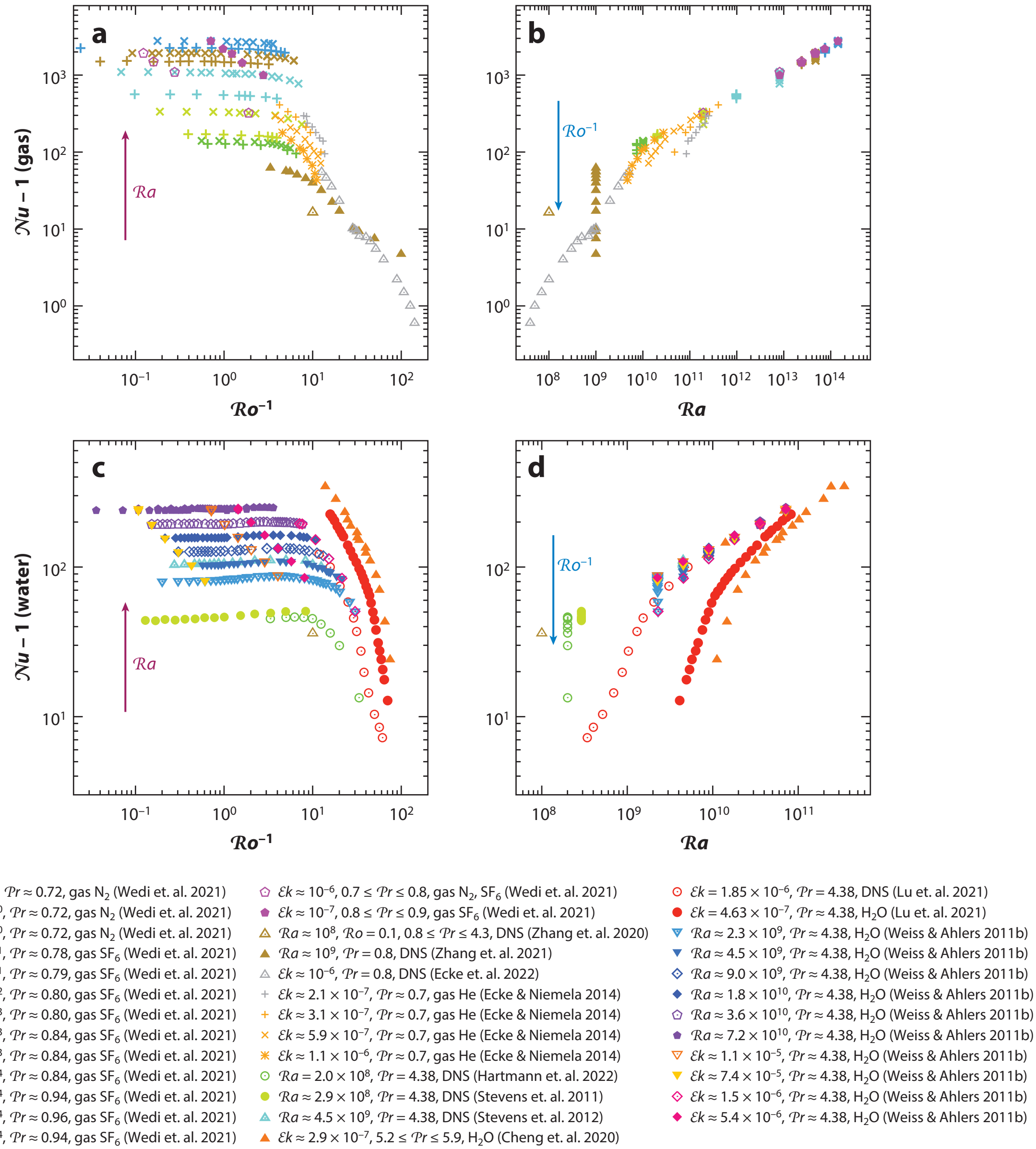

Figure 7

Typical ways to present heat flux measurements in RRBC: (*a*,*c*) for constant temperature difference between the plates Δ (or $\mathcal{R}a$) and varying rotation rate Ω (or $\mathcal{E}k^{-1}$, $\mathcal{R}o^{-1}$) and (*b*,*d*) for constant Ω (or $\mathcal{E}k^{-1}$) and varying Δ (or $\mathcal{R}a$). All shown data are for cylindrical containers with aspect ratio $\Gamma \approx 1/2$ and (*a*,*b*) gases He, N_2, or SF_6 ($0.7 \le \mathcal{P}r \le 0.9$) or (*c*,*d*) water ($4 \le \mathcal{P}r \le 6$). Abbreviation: DNS, direct numerical simulations.

Thus, a larger exponent γ in the buoyancy-dominated regime leads to a larger exponent ξ in the rotation-dominated regime. This relation is illustrated in, for example, **Figure 7*c***: Larger values of $\mathcal{N}u$ in the buoyancy-dominated region at small $\mathcal{R}o^{-1}$ indicate more efficient heat transport with larger values of γ, leading to a steeper decrease of the $\mathcal{N}u$ values in the rotation-dominated regime at large $\mathcal{R}o^{-1}$.

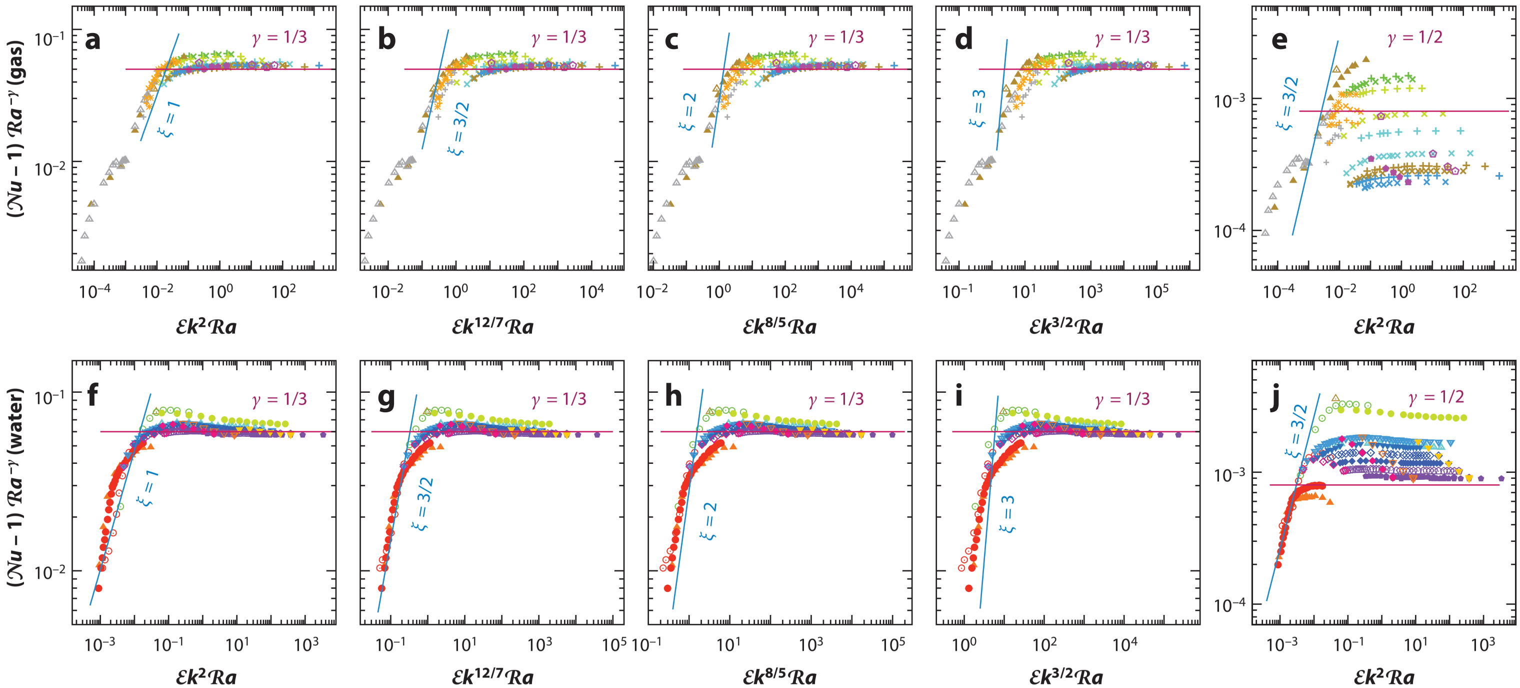

Figure 8

Testing scalings for the transition from $\mathcal{N}u - 1 \sim (\mathcal{R}a/\mathcal{R}a_c)^{\xi}$ (rotation-dominated regime) to $\mathcal{N}u - 1 \sim \mathcal{R}a^{\gamma}$ (buoyancy-dominated regime) using data/symbols from **Figure 7** for (*a*–*e*) gas ($0.7 \le \mathcal{P}r \le 0.9$) and (*f*–*j*) water ($4 \le \mathcal{P}r \le 7$). Slopes $\xi \ge 2$ are too steep for the data (*c*, *d*, *h*–*i*). The horizontal magenta lines indicate the expected buoyancy-dominated scaling and the blue lines show the expected rotation-dominated slopes. Data for gases show $1 < \xi < 3/2$ (*a*,*b*). $\xi = 1$ (*f*) is too small for the water data, whereas $\xi = 3/2$ (*g*,*j*) represents the data well, but the buoyancy-dominated scaling is overestimated by $\gamma \ge 1/3$ (*g*,*e*,*j*).

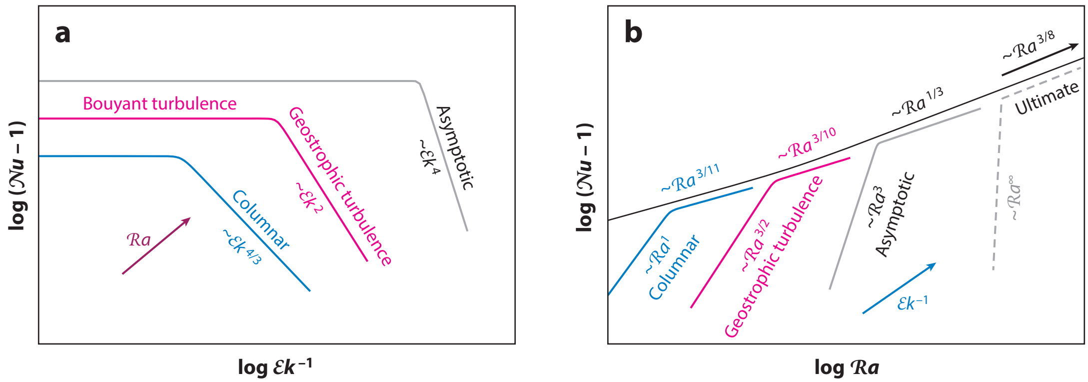

Figure 9

Scalings of $\mathcal{N}u - 1$ versus (*a*) $\mathcal{E}k^{-1}$ and (*b*) $\mathcal{R}a$, according to our theory.

Because of $\lim_{\xi \to \infty} 3\xi/(3 + 8\xi) = 3/8$ and since $3\xi/(3 + 8\xi)$ is a monotonically increasing function for $\xi \geq 0$, we conclude that for extremely large $\mathcal{R}a$, the maximum γ (after transition) is $\gamma = 3/8 = 0.375$. The smallest $\xi = 1$ corresponds to the smallest $\gamma = 3/11 \approx 0.27$ for relatively small $\mathcal{R}a$. The geostrophic turbulence regime with $\xi = 3/2$, which requires larger $\mathcal{R}a$ and $\mathcal{E}k^{-1}$, matches the turbulent buoyancy-dominated regime with $\gamma = 3/10$. Finally, the asymptotic regime with $\xi = 3$, which is only feasible for very large $\mathcal{R}a$ and $\mathcal{E}k^{-1}$, should match $\gamma = 1/3$. Although even higher values of ξ are theoretically possible, they must satisfy $\gamma \leq 3/8$. The proposed scaling relations for $\mathcal{N}u$ versus $\mathcal{E}k^{-1}$ and $\mathcal{R}a$ are presented in **Figure 9**. Once we know how ξ and γ are related (see Equation 11), we can collapse in one plot the data for any specific $\mathcal{P}r$ and Γ by plotting $(\mathcal{N}u - 1)/\mathcal{R}a^{\gamma}$ versus $\mathcal{E}k^{1/(2\gamma)}\mathcal{R}a$, as in **Figure 10*a***. The choice of the *x*-axis follows from the transition happening at constant $\mathcal{E}k^{4\xi/[3(\xi-\gamma)]}\mathcal{R}a = \mathcal{E}k^{1/(2\gamma)}\mathcal{R}a$ (see Equations 10 and 11). If γ (or ξ) is known, then the data should follow a scaling law $(\mathcal{N}u - 1)/\mathcal{R}a^{\gamma} \sim (\mathcal{E}k^{1/(2\gamma)}\mathcal{R}a)^{s}$, as in **Figure 10*a***, showing a slope $s = 0$ in the buoyancy-dominated regime and $s = 8\gamma^2/(3 - 8\gamma)$ in the rotation-dominated regime. The transition then takes place at $\mathcal{R}a \sim \mathcal{E}k^{-1/(2\gamma)}$.

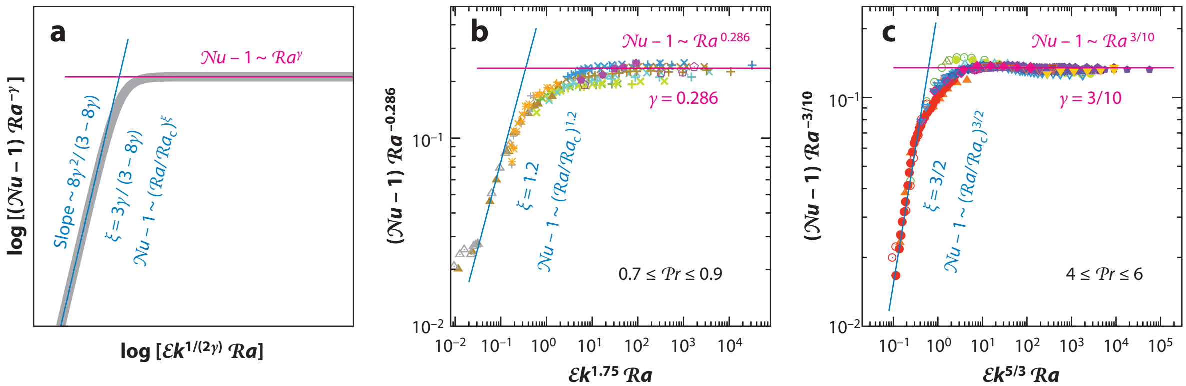

Figure 10

(*a*) Representation of $\mathcal{N}u$ displaying the transition from $\mathcal{N}u - 1 \sim (\mathcal{R}a/\mathcal{R}a_c)^{\xi}$ (rotation-dominated regime) to $\mathcal{N}u - 1 \sim \mathcal{R}a^{\gamma}$ (buoyancy-dominated regime). According to our theory, the scaling exponents ξ and γ follow the relation $\xi = 3\gamma/(3 - 8\gamma)$. (*b*,*c*) Data from **Figure 7**, which are plotted as suggested in panel *a*, for (*b*) $0.7 \leq \mathcal{P}r \leq 0.9$, under the assumptions $\gamma = 2/7 \approx 0.286$ and $\xi = 6/5$ (an intermediate regime between cellular flow and geostrophic turbulence), and (*c*) $4 \leq \mathcal{P}r \leq 6$, under the assumptions $\gamma = 3/10$ and $\xi = 3/2$ (geostrophic turbulence).

For $\Gamma = 1/2$ and $0.7 \le \mathcal{P}r \le 0.9$, **Figure 8*a*,*b*** suggests that ξ satisfies $1 < \xi < 3/2$ with a preference toward 1. If we assume $\xi \approx 6/5$, this would imply $\gamma \approx 2/7 \approx 0.286$ (cf. King et al. 2009). Indeed, all the data from **Figure 7*a*,*b*** begin to follow the same dependence if plotted with $\gamma = 2/7$ and $\xi = 6/5$, as in **Figure 10*b***. Analogously, for $\Gamma = 1/2$ and $4 \le \mathcal{P}r \le 6$, **Figure 8*f*** suggests $\xi = 3/2$, which together with Equation 11 yields $\gamma = 3/10$. Again, all data from **Figure 7*c*,*d***, which are plotted with $\xi = 3/2$ and $\gamma = 3/10$ in **Figure 10*c***, collapse in both the rotation-dominated and buoyancy-dominated regimes. The data plotted in this way not only follow one curve but also support our theoretical conjecture through the relation between slopes in the two regimes (Equation 11). These slopes are indicated by the blue and pink straight lines in **Figure 10*b*,*c***. For $Pr \gtrsim 1$ (**Figure 10*c***), in the rotation-affected regime (for values of $\mathcal{E}k^{5/3}\mathcal{R}a$ slightly above the transitional value, $\mathcal{E}k^{5/3}\mathcal{R}a \gtrsim 0.6$), there is a scatter of the data owing to the Ekman pumping effect, which can lead to $\mathcal{N}u$ values even larger than those in nonrotating RBC. This effect, however, vanishes with increasing $\mathcal{R}a$ and decreasing $\mathcal{P}r$, as discussed above.

There are some caveats to our scaling approach. First, the data for the wall mode regime (seen in the very left of **Figure 10*b***) are ignored in the present analysis. Here we assumed $\mathcal{N}u = 1$ at the onset of bulk convection, whereas wall mode convection, which occurs prior to the bulk convection, can lead to $\mathcal{N}u$ values significantly larger than 1 at $\mathcal{R}a_c$ in the case of small-Γ containers (Ecke et al. 2022, Zhang et al. 2021). Nevertheless, a reduction by 1 or slightly more in the $\mathcal{N}u$ values in plots like **Figure 10*a*** would not significantly influence the scalings, provided $\mathcal{N}u \gg 1$. Second, the values of γ that are chosen to represent the $\mathcal{N}u$ data for small and large $\mathcal{P}r$ in **Figure 10*b*** and **Figure 10*c***, respectively, are, of course, not universal. Here they are chosen empirically, as they better represent the data from **Figure 7**. The values of γ in RRBC vary, in general, between 3/11 and 3/8 and are larger for larger $\mathcal{R}a$. To predict the value of ξ in a particular case, one should first estimate γ in the nonrotating/buoyancy-dominated regime [using the theory of Grossmann & Lohse (2000, 2001)] and then calculate ξ using Equation 11. The data should then collapse onto one master curve if plotted as suggested in **Figure 10*a***. Third, the maximal exponent $\gamma = 3/8$ in buoyancy-dominated RRBC does not contradict the maximal $\gamma \to 1/2$ in nonrotating highly turbulent RBC. In the latter case [as in the regime IV_l of Grossmann & Lohse (2000)], the velocity BL becomes thinner than the thermal BL, which determines the buoyancy-dominated regime in RRBC. Finally, Γ and $\mathcal{F}r$ should also affect the scaling relations, and this needs further investigation. For the data discussed here, $\mathcal{F}r$ is less than 0.15 for both considered $\mathcal{P}r$ ranges, $0.7 \le \mathcal{P}r \le 0.9$ and $4 \le \mathcal{P}r \le 6$. Additionally, Γ is an influential parameter that can shift the principal scaling regimes within the parameter plane (Shishkina 2021, Ahlers et al. 2022), although it acts in a different manner for RRBC owing to wall mode/BZF contributions and to the decreasing horizontal length scale with increasing rotation. Here we mainly discuss the case of $\Gamma = 1/2$. Measurements and DNS data of RRBC in water for a broad range of Γ are given by Lu et al. (2021) and Hartmann et al. (2022).

4. FURTHER TOPICS IN TURBULENT RRBC STUDIES

4.1. Non-Oberbeck–Boussinesq Effects

The validity of the OB approximation in RBC was studied by, for example, Spiegel & Veronis (1960) and Veronis (1962), but most comprehensively by Gray & Giorgini (1976). To derive Equations 1–3 from the continuity, momentum, and energy equations for a Newtonian fluid with zero second viscosity (Batchelor 1967), one assumes (*a*) that all fluid properties are constant except the density in the buoyancy force term in the momentum equation, which is taken to be linearly dependent on the temperature, and (*b*) that the pressure work and the viscous dissipation terms in the heat equation are negligible. The OB validity means that all terms in the residual equations are negligible. Taking a certain small threshold for the residuals, from assumptions *a* and *b* one derives the region of the OB validity in terms of the upper bounds for Δ and H, respectively. The OB validity region for any common fluid is sketched in **Figure 4*a***. Thus, within the OB validity region for any reasonable threshold, both Δ and $H < C\Delta$ are bounded, where C depends on the fluid properties alone. This means that for any chosen fluid, $\mathcal{Ra}$ larger than a certain value will no longer satisfy the OB criterion. This is a problem that RRBC and nonrotating RBC share.

Non-OB effects in RRBC in water, where the fluid properties are considered temperature dependent, have been studied by Horn & Shishkina (2014). Without rotation, the non-OB effects lead to a global asymmetry of the flow, which is reflected, in particular, in an increased bulk temperature. With increasing rotation, the central temperature approaches that of the OB case, but the asymmetry of the BLs remains.

4.2. Centrifugal Buoyancy Effects

Centrifugal buoyancy changes the flow structure and the response characteristics in RRBC (Homsy & Hudson 1971). This holds for both the buoyancy-dominated and rotation-dominated regimes. For example, in a weakly nonlinear rotation-dominated regime, the complex Ginzburg–Landau equation (van Saarloos & Hohenberg 1992, Aranson & Kramer 2002) predicts the scalings of the correlation length as $\sim\epsilon^{-1/2}$ and precession frequency as $\sim\epsilon^{1}$, which is also consistent with the numerical solutions of the Swift–Hohenberg equation (Cross et al. 1994). Measurements by Hu et al. (1995, 1998) for large $\Gamma = 46$ and 80, however, deviate from these theoretical predictions, suggesting scaling exponents that are about two times smaller in both cases. Simulations by Becker et al. (2006) have clarified this discrepancy: They show that if the centrifugal term is removed from the momentum equation, the numerical results are consistent with theory (which neglects the centrifugal buoyancy), but inclusion of the centrifugal term leads to results consistent with experiments. Note that the derivation of an OB amplitude equation that includes the centrifugation is nontrivial, as the required toroidal-poloidal decomposition cannot adjust the radial dependency (see Küppers & Lortz 1969, Knobloch 1998, Marques et al. 2007, Scheel 2007, Scheel et al. 2010).

In DNS by Horn & Aurnou (2018, 2019, 2021) and in experiments by Hu et al. (2021, 2022), centrifugal buoyancy effects were investigated over broad ranges of $\mathcal{Ro}$ and $\mathcal{Fr}$. Centrifugal buoyancy causes warm (cold) fluid near the bottom (top) plate to move inward (outward) from the centerline with downward flow at the sidewalls, which leads to strongly asymmetric mean temperature profiles in the vertical and radial directions: In the core part of the domain the fluid is always warmer along the centerline than it is near the sidewalls (Hart 2000, Horn & Aurnou 2019). These effects increase with increasing $\mathcal{Fr}$. Horn & Aurnou (2018, 2019) suggested different rotation-dominated regimes in centrifugal buoyancy where the flow can be quasi-geostrophic or quasi-cyclostrophic such that the primary force balance is between the pressure gradient and the Coriolis force or centrifugal buoyancy, respectively. In the cyclostrophic state, tornado-like large-scale structures can form. A triple balance between pressure gradient, Coriolis, and centrifugal forces gives the so-called gradient wind balance, which is particularly important in tropical cyclones (Willoughby 1990).

Different regimes of the dominance of gravitational or centrifugal buoyancy, or of Coriolis forces, can be extracted by analyzing the corresponding timescales τ_{ff}, τ_{c}, and τ_{Ω} in each regime (see the sidebar titled Dimensional Characteristics of Rotating RRBC): The smallest timescale determines the dominance of the corresponding force. Transitions between the regimes are determined by equating the timescales of the neighboring regimes. This way one obtains regime diagrams, as in **Figure 11**. The dominance of centrifugation over buoyancy is expected for

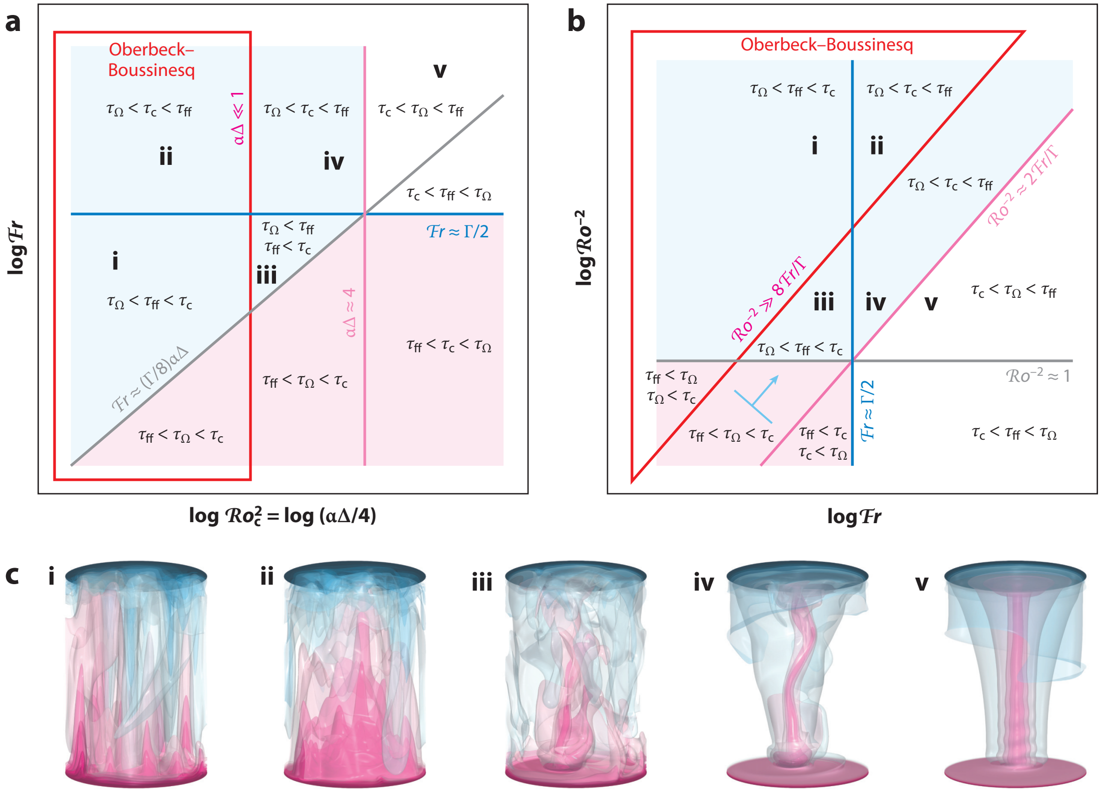

Figure 11

Phase diagrams of RRBC with centrifugal effects, in terms of (*a*) $\mathcal{F}r$ and $\mathcal{R}o_c \equiv \sqrt{\alpha\Delta}/2$, where α is the thermal expansion coefficient and Δ is the temperature difference between the plates, and (*b*) $\mathcal{F}r$ and $\mathcal{R}o$. Buoyancy-, Coriolis-, and centrifugal-dominated regimes are shown with pink, blue, and white shading, respectively. This is determined by the smallest timescales in the regimes τ_{ff}, τ_Ω, or τ_c (see the sidebar titled Dimensional Characteristics of RRBC for definitions). According to Hu et al. (2022), centrifugal effects become apparent earlier, at $\mathcal{F}r \sim \mathcal{R}a^{0.5}$ (*light blue line with arrow*). Regions of the Oberbeck–Boussinesq validity, according to Gray & Giorgini (1976), are marked with dark magenta lines. Examples of temperature fields (after Horn & Aurnou 2018) marked as subpanels *i*–*v* in panels *a* and *b* are presented in panel *c* for $\mathcal{R}a = 10^8$, $\mathcal{P}r = 6.52$, and $\Gamma = 0.73$ and for the following values: (*i*) $\mathcal{R}o^{-1} = 20$ and $\mathcal{F}r = 0.1$ ($\alpha\Delta \approx 2.7 \times 10^{-3}$, $\mathcal{E}k \approx 1.3 \times 10^{-5}$), (*ii*) $\mathcal{R}o^{-1} = 20$ and $\mathcal{F}r = 0.5$ ($\alpha\Delta \approx 1.4 \times 10^{-2}$, $\mathcal{E}k \approx 1.3 \times 10^{-5}$), (*iii*) $\mathcal{R}o^{-1} = 2$ and $\mathcal{F}r = 0.1$ ($\alpha\Delta \approx 2.7 \times 10^{-1}$, $\mathcal{E}k \approx 1.3 \times 10^{-4}$), (*iv*) $\mathcal{R}o^{-1} = 2$ and $\mathcal{F}r = 0.5$ ($\alpha\Delta \approx 1.4$ and $\mathcal{E}k \approx 1.3 \times 10^{-4}$), and (*v*) $\mathcal{R}o^{-1} = 2$ and $\mathcal{F}r = 2$ ($\alpha\Delta \approx 5.5$, $\mathcal{E}k \approx 1.3 \times 10^{-4}$).

$\mathcal{F}r > \Gamma/2$ (the transition is marked in **Figure 11**). For a given cell height H, only the rotation rate Ω determines the onset of centrifugal dominance, and not the aspect ratio Γ, since $\mathcal{F}r > \Gamma/2$ implies $\Omega^2 H/g > 1$. Experiments by Hu et al. (2022) show, however, that the centrifugal effects become apparent much earlier (at $\mathcal{F}r \sim \mathcal{R}a^{0.5}$); this is indicated in **Figure 11*b***. The dominance of the centrifugal over Coriolis force occurs for $\mathcal{R}o_c > 1$ (**Figure 11**), which means that this region lies outside the region of the OB validity, given $\mathcal{R}o_c = \sqrt{\alpha\Delta}/2$. Thus, to study in DNS regimes dominated by centrifugation, one is forced to consider non-OB governing equations. Another feature is that the gravitational buoyancy time considered here is universally based on H and the free-fall velocity u_{ff}. This implies that for any small $\mathcal{F}r$, the transition from the rotation-dominated to the buoyancy-dominated regime always takes place at a constant $\mathcal{R}o^{-1}$. As we have seen in Section 3.3, however, this is not universal; thus a further inspection of the phenomena of centrifugal effects in RRBC is needed.

4.3. Boundary Conditions in RRBC

Schmitz & Tilgner (2010), Stellmach et al. (2014), and Kunnen et al. (2016) showed in different simulations for a broad range of $\mathcal{E}k$ that free-slip BCs at the plates lead to several times smaller values of $\mathcal{N}u$. The no-slip BCs at the plate allow the formation of the Ekman BLs; thus, Ekman pumping leads to more efficient heat transport in large-$\mathcal{P}r$ fluids. This effect is also reflected in simulations using the extended asymptotic model with the Ekman pumping BCs (Plumley et al. 2017). DNS by Kunnen et al. (2016) for different BCs at the plates, for the same $\mathcal{R}a \approx 10^{10}$ and $\mathcal{E}k \approx 10^{-6}$, showed that the flows with the free-slip BCs follow the geostrophic turbulence scaling $\mathcal{N}u \sim \mathcal{E}k^2$, whereas flows with no-slip BCs still follow the scaling $\mathcal{N}u \sim \mathcal{E}k^{1.2}$, which indicates that the transitions between different regimes in RRBC depend on the BCs at the plates (for the no-slip case, a higher $\mathcal{R}a$ is required). For the same control parameters in the simulations with no-slip and free-slip BCs, Stellmach et al. (2014) and Kunnen et al. (2016) observed the formation of large-scale vortices only in the former case. Aguirre Guzmán et al. (2020) showed that large-scale vortices are formed for the no-slip BCs for larger $\mathcal{R}a/\mathcal{R}a_c$ values than are required for the free-slip case.

SUMMARY POINTS

1. The nonhydrostatic quasi-geostrophic model gives a compelling qualitative description of rotation-dominated rotating Rayleigh-Bénard Convection (RRBC), but how it breaks down as $\mathcal{R}a/\mathcal{R}a_c$ increases, including the role of Ekman pumping and turbulent boundary layers, remains unresolved quantitatively. Although there is much evidence accumulating during a very active campaign by multiple groups worldwide, there remain significant questions about both heat transport and local quantities of RRBC.
2. The phenomenology of heat transport scaling in rotation-dominated and buoyancy-dominated regimes that we introduced in Section 3.3 and **Figure 10*a*** expresses how the crossover from scaling in one domain puts limits on the scaling in the other. The boundaries of different qualitative domains remain somewhat uncertain.
3. The Oberbeck–Boussinesq (OB) validity region is quite restricted for any fluid (**Figure 4**). Large H, Δ, or Ω unavoidably leads to nonnegligible non-OB effects. It seems that in both direct numerical simulations (DNS) and experiments, we have arrived at the limits of the OB approximation in RRBC and in nonrotating RBC, and proper adjustments of the governing equations are needed.
4. The presence of remnant wall modes and boundary zonal flow (BZF) in experiments on RRBC poses interesting challenges to separate the contributions of the BZF from the bulk RRBC convection process. Understanding the contributions of each will improve our understanding of both in realistic containers.

FUTURE ISSUES

1. The great challenge of laboratory and DNS investigations of RRBC is determining which aspects of the model system are applicable to similar problems in geophysical and astrophysical manifestations of RRBC, such as the outer core of the Earth and the

convective zone of stars. We are partway along that path, but incorporating more realistic governing equations, geometries, and boundary conditions and exploring a broader parameter range remain exciting challenges for the future.

2. The experimental challenges for the future remain being able to fully probe the domain of quasi-geostrophic RRBC while maintaining the asymptotic conditions associated with the model. Better experiments are being developed, and the measurement tools are becoming increasingly powerful. DNS continue to push the envelope of extended range and flexibility. The next decade should be an exciting one for advances in RRBC.

DISCLOSURE STATEMENT

The authors are not aware of any biases that might be perceived as affecting the objectivity of this review.

ACKNOWLEDGMENTS

We would like to thank all our colleagues and collaborators on RRBC over many years. We appreciate contributions to this review by J. Aurnou, J. Cheng, R. Hartmann, K. Julien, R. Kunnen, D. Lohse, R. Stevens, S. Weiss, X. Zhang, and J.-Q. Zhong, who provided additional data and explanations. For invaluable moral support, O.S. expresses her gratitude to E. Bodenschatz, S. Eckert, S. Grossmann, D. Lohse, A. Navalny, and V. Zelensky. R.E.E. acknowledges support from the US Department of Energy and the Los Alamos National Laboratory LDRD (Laboratory-Directed Research & Development) program.

LITERATURE CITED

Aguirre Guzmán AJ, Madonia M, Cheng JS, Ostilla-Mónico R, Clercx HJH, Kunnen RPJ. 2020. Competition between Ekman plumes and vortex condensates in rapidly rotating thermal convection. *Phys. Rev. Lett.* 125(21):214501

Aguirre Guzmán AJ, Madonia M, Cheng JS, Ostilla-Mónico R, Clercx HJH, Kunnen RPJ. 2021. Force balance in rapidly rotating Rayleigh–Bénard convection. *J. Fluid Mech.* 928:A16

Aguirre Guzmán AJ, Madonia M, Cheng JS, Ostilla-Mónico R, Clercx HJH, Kunnen RPJ. 2022. Flow- and temperature-based statistics characterizing the regimes in rapidly rotating turbulent convection in simulations employing no-slip boundary conditions. *Phys. Rev. Fluids* 7:013501

Ahlers G, Bodenschatz E, Hartmann R, He X, Lohse D, et al. 2022. Aspect ratio dependence of heat transfer in a cylindrical Rayleigh–Bénard cell. *Phys. Rev. Lett.* 128:084501

Ahlers G, Funfschilling D, Bodenschatz E. 2009a. Transitions in heat transport by turbulent convection at Rayleigh numbers up to 10^{15}. *New J. Phys.* 11:123001

Ahlers G, Grossmann S, Lohse D. 2009b. Heat transfer and large scale dynamics in turbulent Rayleigh–Bénard convection. *Rev. Mod. Phys.* 81:503–37

Aranson IS, Kramer L. 2002. The world of the complex Ginzburg–Landau equation. *Rev. Mod. Phys.* 74:99–143

Aurnou JM, Bertin V, Grannan AM, Horn S, Vogt T. 2018. Rotating thermal convection in liquid gallium: multi-modal flow, absent steady columns. *J. Fluid Mech.* 846:846–76

Aurnou JM, Horn S, Julien K. 2020. Connections between nonrotating, slowly rotating, and rapidly rotating turbulent convection transport scalings. *Phys. Rev. Res.* 2(4):043115

Aurnou JM, Olson P. 2001. Strong zonal winds generated by thermal convection in rotating spherical shells. *Geophys. Res. Lett.* 28:2557–59

Bassom AP, Zhang K. 1994. Strongly nonlinear convection cells in a rapidly rotating fluid layer. *Geophys. Astrophys. Fluid Dyn.* 76:223–38

Batchelor GK. 1967. *An Introduction to Fluid Dynamics*. Cambridge, UK: Cambridge Univ. Press
Becker N, Scheel JD, Cross MC, Ahlers G. 2006. Effect of the centrifugal force on domain chaos in Rayleigh–Bénard convection. *Phys. Rev. E* 73:066309
Boffetta G, Ecke RE. 2012. Two-dimensional turbulence. *Annu. Rev. Fluid Mech.* 44:427–51
Boubnov BM, Golitsyn GS. 1986. Experimental study of convective structures in rotating fluids. *J. Fluid Mech.* 167:503–31
Boubnov BM, Golitsyn GS. 1995. *Convection in Rotating Fluids*. Dordrecht, Neth.: Springer Sci. Bus. Media
Bouillaut V, Miquel B, Julien K, Aumaître S, Gallet B. 2021. Experimental observation of the geostrophic turbulence regime of rapidly rotating convection. *PNAS* 118:e2105015118
Boussinesq J. 1903. *Théorie analytique de la chaleur*. Paris: Gauthier-Villars
Buell JC, Catton I. 1983. The effect of wall conduction on the stability of a fluid in a right circular cylinder heated from below. *J. Heat Transf.* 105:255–60
Busse FH. 2002. Convective flows in rapidly rotating spheres and their dynamo action. *Phys. Fluids* 14:1301
Canuto VM, Dubovikov MS. 1998. Two scaling regimes for rotating Rayleigh–Bénard convection. *Phys. Rev. Lett.* 80(2):281–84
Chandrasekhar S. 1953. The instability of a layer of fluid heat below and subject to Coriolis forces. *Proc. R. Soc. Lond. A* 217:306–27
Chandrasekhar S. 1961. *Hydrodynamic and Hydromagnetic Stability*. Oxford: Clarendon Press
Cheng JS, Aurnou JM, Julien K, Kunnen RPJ. 2018. A heuristic framework for next-generation models of geostrophic convective turbulence. *Geophys. Astrophys. Fluid Dyn.* 112:277–300
Cheng JS, Madonia M, Aguirre Guzmán AJ, Kunnen RPJ. 2020. Laboratory exploration of heat transfer regimes in rapidly rotating turbulent convection. *Phys. Rev. Fluids* 5(11):113501
Cheng JS, Stellmach S, Ribeiro A, Grannan A, King EM, Aurnou JM. 2015. Laboratory-numerical models of rapidly rotating convection in planetary cores. *Geophys. J. Int.* 201:1–17
Chong KL, Shi JQ, Ding SS, Ding GY, Lu HY, et al. 2020. Vortices as Brownian particles in turbulent flows. *Sci. Adv.* 6:aaz1110
Chong KL, Yang Y, Huang SD, Zhong JQ, Stevens RJAM, et al. 2017. Confined Rayleigh–Bénard, rotating Rayleigh–Bénard, and double diffusive convection: a unifying view on turbulent transport enhancement through coherent structure manipulation. *Phys. Rev. Lett.* 119(6):064501
Cioni S, Ciliberto S, Sommeria J. 1997. Strongly turbulent Rayleigh–Bénard convection in mercury: comparison with results at moderate Prandtl number. *J. Fluid Mech.* 335:111–40
Cox SM, Matthews PC. 2000. Instability of rotating convection. *J. Fluid Mech.* 403:153–72
Cross MC, Meiron D, Tu Y. 1994. Chaotic domains: a numerical investigation. *Chaos* 4:607–19
Dawes J. 2001. Rapidly rotating thermal convection at low Prandtl number. *J. Fluid Mech.* 428:61–80
de Wit XM, Aguirre Guzmán AJ, Madonia M, Cheng JS, Clercx HJH, Kunnen RPJ. 2020. Turbulent rotating convection confined in a slender cylinder: the sidewall circulation. *Phys. Rev. Fluids* 5(2):023502
de Wit XM, Aguirre Guzmán AJ, Madonia M, Cheng JS, Clercx HJH, Kunnen RPJ. 2022. Discontinuous transitions towards vortex condensates in buoyancy-driven rotating turbulence. *J. Fluid Mech.* 963:A43
Ding SS, Chong KL, Shi JQ, Ding GY, Lu HY, et al. 2021. Inverse centrifugal effect induced by collective motion of vortices in rotating thermal convection. *Nat. Commun.* 12:5585
Ding SS, Li HM, Yan WD, Zhong JQ. 2019. Temperature fluctuations relevant to thermal-plume dynamics in turbulent rotating Rayleigh–Bénard convection. *Phys. Rev. Fluids* 4:023501
Ecke RE. 2015. Scaling of heat transport near onset in rapidly rotating convection. *Phys. Lett. A* 379:2221–23
Ecke RE, Niemela JJ. 2014. Heat transport in the geostrophic regime of rotating Rayleigh–Bénard convection. *Phys. Rev. Lett.* 113:114301
Ecke RE, Zhang X, Shishkina O. 2022. Connecting wall modes and boundary zonal flows in rotating Rayleigh–Bénard convection. *Phys. Rev. Fluids* 7:L011501
Ecke RE, Zhong F, Knobloch E. 1992. Hopf bifurcation with broken reflection symmetry in rotating Rayleigh–Bénard convection. *Europhys. Lett.* 19(3):177–82
Favier B, Guervilly C, Knobloch E. 2019. Subcritical turbulent condensate in rapidly rotating Rayleigh–Bénard convection. *J. Fluid Mech.* 864:R1
Favier B, Knobloch E. 2020. Robust wall states in rapidly rotating Rayleigh–Bénard convection. *J. Fluid Mech.* 895:R1

Favier B, Silvers LJ, Proctor MRE. 2014. Inverse cascade and symmetry breaking in rapidly rotating Boussinesq convection. *Phys. Fluids* 26:096605

Fernando HJS, Chen RR, Boyer DL. 1991. Effects of rotation on convective turbulence. *J. Fluid Mech.* 228:513–47

Fischer PF. 1997. An overlapping Schwartz method for spectral element solutions of the incompressible Navier-Stokes equations. *J. Comput. Phys.* 133:84–101

Funfschilling D, Ahlers G. 2004. Plume motion and large-scale dynamics in a cylindrical Rayleigh–Bénard cell. *Phy. Rev. Lett.* 92:194502

Gastine T, Wicht J, Aubert J. 2016. Scaling regimes in spherical shell rotating convection. *J. Fluid Mech.* 808:690–732

Glatzmaier GA. 2014. *Introduction to Modeling Convection in Planets and Stars: Magnetic Field, Density Stratification, Rotation*. Princeton, NJ: Princeton Univ. Press

Goldstein HF, Knobloch E, Mercader I, Net M. 1993. Convection in a rotating cylinder. Part 1 Linear theory for moderate Prandtl numbers. *J. Fluid Mech.* 248:583–604

Grannan AM, Cheng JS, Aggarwal A, Hawkins EK, Xu Y, et al. 2022. Experimental pub crawl from Rayleigh–Bénard to magnetostrophic convection. *J. Fluid Mech.* 939:R1

Gray DD, Giorgini A. 1976. The validity of the Boussinesq approximation for liquids and gases. *Int. J. Heat Mass Transf.* 19:545–51

Greenspan HP. 1968. *The Theory of Rotating Fluids*. Cambridge, UK: Cambridge Univ. Press

Grooms I, Julien K, Weiss JB, Knobloch E. 2010. Model of convective Taylor columns in rotating Rayleigh–Bénard convection. *Phys. Rev. Lett.* 104(22):224501

Grooms I, Whitehead J. 2014. Bounds on heat transport in rapidly rotating Rayleigh–Bénard convection. *Nonlinearity* 28:29–41

Grossmann S, Lohse D. 2000. Scaling in thermal convection: a unifying theory. *J. Fluid Mech.* 407:27–56

Grossmann S, Lohse D. 2001. Thermal convection for large Prandtl numbers. *Phys. Rev. Lett.* 86:3316–19

Guervilly C, Cardin P. 2016. Subcritical convection of liquid metals in a rotating sphere using a quasi-geostrophic model. *J. Fluid Mech.* 808:61–89

Guervilly C, Hughes DW. 2017. Jets and large-scale vortices in rotating Rayleigh–Bénard convection. *Phys. Rev. Fluids* 2(11):113503

Guervilly C, Hughes DW, Jones C. 2014. Large-scale vortices in rapidly rotating Rayleigh–Bénard convection. *J. Fluid Mech.* 758:407–35

Hart JE. 2000. On the influence of centrifugal buoyancy on rotating convection. *J. Fluid Mech.* 403:133–51

Hart JE, Kittelman S, Ohlsen DR. 2002. Mean flow precession and temperature probability density functions in turbulent rotating convection. *Phys. Fluids* 14:955

Hart JE, Ohlsen DR. 1999. On the thermal offset in turbulent rotating convection. *Phys. Fluids* 11:2101–7

Hartmann R, Verzicco R, Kranenbarg LK, Lohse D, Stevens RJAM. 2022. Multiple heat transport maxima in confined rotating Rayleigh–Bénard convection. *J. Fluid Mech.* 939:A1

Heard WB, Veronis G. 1971. Asymptotic treatment of the stability of a rotating layer of fluid with rigid boundaries. *Geophys. Fluid Dyn.* 2:299–316

Herrmann J, Busse FH. 1993. Asymptotic theory of wall-attached convection in a rotating fluid layer. *J. Fluid Mech.* 255:183–94

Homsy G, Hudson J. 1971. Centrifugal convection and its effect on the asymptotic stability of a bounded rotating fluid heated from below. *J. Fluid Mech.* 48:605–24

Horn S, Aurnou JM. 2018. Regimes of Coriolis-centrifugal convection. *Phys. Rev. Lett.* 120:204502

Horn S, Aurnou JM. 2019. Rotating convection with centrifugal buoyancy: numerical predictions for laboratory experiments. *Phys. Rev. Fluids* 4:073501

Horn S, Aurnou JM. 2021. Tornado-like vortices in the quasi-cyclostrophic regime of Coriolis-centrifugal convection. *J. Turbulence* 22:297–324

Horn S, Schmid PJ. 2017. Prograde, retrograde, and oscillatory modes in rotating Rayleigh–Bénard convection. *J. Fluid Mech.* 831:182–211

Horn S, Shishkina O. 2014. Rotating non-Oberbeck–Boussinesq Rayleigh–Bénard convection in water. *Phys. Fluids* 26:055111

Horn S, Shishkina O. 2015. Toroidal and poloidal energy in rotating Rayleigh–Bénard convection. *J. Fluid Mech.* 762:232–55

Hu Y, Ecke R, Ahlers G. 1995. Time and length scales in rotating Rayleigh–Bénard convection. *Phys. Rev. Lett.* 74(25):5040–43

Hu Y, Pesch W, Ahlers G, Ecke R. 1998. Convection under rotation for Prandtl numbers near 1: Küppers–Lortz instability. *Phys. Rev. E* 58(5):5821–33

Hu YB, Huang SD, Xie YC, Xia KQ. 2021. Centrifugal-force-induced flow bifurcations in turbulent thermal convection. *Phys. Rev. Lett.* 127:244501

Hu YB, Xie YC, Xia KQ. 2022. On the centrifugal effect in turbulent rotating thermal convection: inset and heat transport. *J. Fluid Mech.* 938:R1

Julien K, Aurnou JM, Calkins MA, Knobloch E, Marti P, et al. 2016. A nonlinear model for rotationally constrained convection with Ekman pumping. *J. Fluid Mech.* 798:50–87

Julien K, Knobloch E, Plumley M. 2018. Impact of domain anisotropy on the inverse cascade in geostrophic turbulent convection. *J. Fluid Mech.* 837:R4

Julien K, Knobloch E, Rubio AM, Vasil GM. 2012a. Heat transport in low-Rossby-number Rayleigh–Bénard convection. *Phys. Rev. Lett.* 109:254503

Julien K, Legg S, McWilliams J, Werne J. 1996. Rapidly rotating turbulent Rayleigh–Bénard convection. *J. Fluid Mech.* 322:243–73

Julien K, Rubio AM, Grooms I, Knobloch E. 2012b. Statistical and physical balances in low Rossby number Rayleigh–Bénard convection. *Geophys. Astrophys. Fluid Dyn.* 106(4–5):392–428

Kaplan EJ, Schaeffer N, Vidal J, Cardin P. 2017. Subcritical thermal convection of liquid metals in a rapidly rotating sphere. *Phys. Rev. Lett.* 119:094501

King EM, Aurnou JM. 2012. Thermal evidence for Taylor columns in turbulent rotating Rayleigh–Bénard convection. *Phys. Rev. E* 85:016313

King EM, Aurnou JM. 2013. Turbulent convection in liquid metal with and without rotation. *PNAS* 110:6688–93

King EM, Stellmach S, Aurnou JM. 2012. Heat transfer by rapidly rotating Rayleigh–Bénard convection. *J. Fluid Mech.* 691:568–82

King EM, Stellmach S, Buffett B. 2013. Scaling behaviour in Rayleigh–Bénard convection with and without rotation. *J. Fluid Mech.* 717:449–71

King EM, Stellmach S, Noir J, Hansen U, Aurnou JM. 2009. Boundary layer control of rotating convection systems. *Nature* 457:301–4

Knobloch E. 1998. Rotating convection: recent developments. *Int. J Eng. Sci.* 36(12–14):30

Kooij GL, Botchev MA, Frederix EM, Geurts BJ, Horn S, et al. 2018. Comparison of computational codes for direct numerical simulations of turbulent Rayleigh–Bénard convection. *Comput. Fluids* 166:1–8

Kraichnan R. 1962. Turbulent thermal convection at arbitrary Prandtl number. *Phys. Fluids* 5:1374–89

Kunnen RPJ. 2021. The geostrophic regime of rapidly rotating turbulent convection. *J. Turbulence* 22(4–5):267–96

Kunnen RPJ, Clercx HJH, Geurts BJ. 2008. Breakdown of large-scale circulation in turbulent rotating convection. *Europhys. Lett.* 84:24001

Kunnen RPJ, Clercx HJH, van Heijst GF. 2013. The structure of sidewall boundary layers in confined rotating Rayleigh–Bénard convection. *J. Fluid Mech.* 727:509–32

Kunnen RPJ, Geurts BJ, Clercx HJH. 2009. Turbulence statistics and energy budget in rotating Rayleigh-Bénard convection. *Eur. J. Mech. B/Fluids* 28:579–89

Kunnen RPJ, Geurts BJ, Clercx HJH. 2010a. Experimental and numerical investigation of turbulent convection in a rotating cylinder. *J. Fluid Mech.* 642:445–76

Kunnen RPJ, Geurts BJ, Clercx HJH. 2010b. Vortex statistics in turbulent rotating convection. *Phys. Rev. E* 82:036306

Kunnen RPJ, Ostilla-Mónico R, der Poel EV, Verzicco R, Lohse D. 2016. Transition to geostrophic convection: the role of the boundary conditions. *J. Fluid Mech.* 799:413–32

Kunnen RPJ, Stevens RJAM, Overkamp J, Sun C, van Heijst GF, Clercx HJH. 2011. The role of Stewartson and Ekman layers in turbulent rotating Rayleigh–Bénard convection. *J. Fluid Mech.* 688:422–42

Kuo EY, Cross MC. 1993. Traveling-wave wall states in rotating Rayleigh–Bénard convection. *Phys. Rev. E* 47:R2245–R2248

Küppers G, Lortz D. 1969. Transition from laminar convection to thermal turbulence in a rotating fluid layer. *J. Fluid Mech.* 35(3):609–20

Liu Y, Ecke RE. 1997. Heat transport scaling in turbulent Rayleigh–Bénard convection: effects of rotation and Prandtl number. *Phys. Rev. Lett.* 79:2257

Liu Y, Ecke RE. 2009. Heat transport measurements in turbulent Rayleigh–Bénard convection. *Phys. Rev. E* 80:036314

Liu Y, Ecke RE. 2011. Local temperature measurements in turbulent Rayleigh–Bénard convection. *Phys. Rev. E* 84:016311

Long R, Mound J, Davies C, Tobias S. 2020. Scaling behaviour in spherical shell rotating convection with fixed-flux thermal boundary conditions. *J. Fluid Mech.* 889:A7

Lopez JM, Marques F. 2009. Centrifugal effects in rotating convection: nonlinear dynamics. *J. Fluid Mech.* 628:269–97

Lu HY, Ding GY, Shi JQ, Xia KQ, Zhong JQ. 2021. Heat-transport scaling and transition in geostrophic rotating convection with varying aspect ratio. *Phys. Rev. Fluids* 6(7):L071501

Lucas PGJ, Pfotenhauer JM, Donnelly RJ. 1983. Stability and heat transfer of rotating cryogens. Part 1. Influence of rotation on the onset of convection in liquid ^{4}He. *J. Fluid Mech.* 129:251–64

Maffei S, Krouss M, Julien K, Calkins M. 2021. On the inverse cascade and flow speed scaling behaviour in rapidly rotating Rayleigh–Bénard convection. *J. Fluid Mech.* 913:A18

Malkus MVR. 1954. The heat transport and spectrum of thermal turbulence. *Proc. R. Soc. Lond. A* 225:196–212

Marques F, Mercader I, Batiste O, Lopez JM. 2007. Centrifugal effects in rotating convection: axisymmetric states and three-dimensional instabilities. *J. Fluid Mech.* 580:303–18

Nakagawa Y, Frenzen P. 1955. A theoretical and experimental study of cellular convection in rotating fluids. *Tellus* 7:2–21

Niemela JJ, Babuin S, Sreenivasan KR. 2010. Turbulent rotating convection at high Rayleigh and Taylor numbers. *J. Fluid Mech.* 649:509–22

Niemela JJ, Skrbek L, Sreenivasan KR, Donnelly RJ. 2000. Turbulent convection at very high Rayleigh numbers. *Nature* 404:837–41

Nieves D, Rubio AM, Julien K. 2014. Statistical classification of flow morphology in rapidly rotating Rayleigh–Bénard convection. *Phys. Fluids* 26:086602

Niiler PP, Bisshopp FE. 1965. On the influence of Coriolis force on onset of thermal convection. *J. Fluid Mech.* 22(4):753–61

Ning L, Ecke R. 1993. Rotating Rayleigh–Bénard convection: aspect-ratio dependence of the initial bifurcations. *Phys. Rev. E* 47(5):3326–33

Noto D, Tasaka Y, Yanagisawa T, Murai Y. 2019. Horizontal diffusive motion of columnar vortices in rotating Rayleigh–Bénard convection. *J. Fluid Mech.* 871:401–26

Oberbeck A. 1879. Über die Wärmeleitung der Flüssigkeiten bei Berücksichtigung der Strömungen in Folge von Temperaturdifferenzen. *Ann. Phys.* 243(6):271–92

Pedlosky J. 1987. *Geophysical Fluid Dynamics*. New York: Springer-Verlag. 2nd ed.

Pfotenhauer JM, Niemela JJ, Donnelly RJ. 1987. Stability and heat transfer of rotating cryogens. Part 3. Effects of finite cylindrical geometry and rotation on the onset of convection. *J. Fluid Mech.* 175:85–96

Plumley M, Julien K. 2019. Scaling laws in Rayleigh–Bénard convection. *Earth Space Sci.* 6(9):1580–92

Plumley M, Julien K, Marti P, Stellmach S. 2016. The effects of Ekman pumping on quasi-geostrophic Rayleigh–Bénard convection. *J. Fluid Mech.* 803:51–71

Plumley M, Julien K, Marti P, Stellmach S. 2017. Sensitivity of rapidly rotating Rayleigh–Bénard convection to Ekman pumping. *Phys. Rev. Fluids* 2:094801

Priestley CHB. 1959. *Turbulent Transfer in the Lower Atmosphere*. Chicago: Univ. Chicago Press

Proudman J. 1916. On the motion of solids in a liquid possessing vorticity. *Proc. R. Soc. Lond. A* 92:408–24

Rajaei H, Joshi P, Alards KMJ, Kunnen RPJ, Toschi F, Clercx HJH. 2016. Transitions in turbulent rotating convection: a Lagrangian perspective. *Phys. Rev. E* 93(4):043129

Rajaei H, Kunnen RPJ, Clercx HJH. 2017. Exploring the geostrophic regime of rapidly rotating convection with experiments. *Phys. Fluids* 29:045105

Rossby TH. 1969. A study of Bénard convection with and without rotation. *J. Fluid Mech.* 36:309–35

Rubio AM, Julien K, Knobloch E, Weiss JB. 2014. Upscale energy transfer in three-dimensional rapidly rotating turbulent convection. *Phys. Rev. Lett.* 112(14):144501

Sakai S. 1997. The horizontal scale of rotating convection in the geostrophic regime. *J. Fluid Mech.* 333:85–95

Scheel JD. 2007. The amplitude equation for rotating Rayleigh–Bénard convection. *Phys. Fluids* 19:104105

Scheel JD, Mutyaba PL, Kimmel T. 2010. Patterns in rotating Rayleigh–Bénard convection at high rotation rates. *J. Fluid Mech.* 659:24–42

Scheel JD, Paul MR, Cross MC, Fischer P. 2003. Traveling waves in rotating Rayleigh–Bénard convection: analysis of modes and mean flow. *Phys. Rev. E* 68(6):066216

Schmitz S, Tilgner A. 2009. Heat transport in rotating convection without Ekman layers. *Phys. Rev. E* 80(1):015305

Schmitz S, Tilgner A. 2010. Transitions in turbulent rotating Rayleigh–Bénard convection. *Geophys. Astrophys. Fluid Dyn.* 104:481–89

Shi JQ, Lu HY, Ding SS, Zhong JQ. 2020. Fine vortex structure and flow transition to the geostrophic regime in rotating Rayleigh–Bénard convection. *Phys. Rev. Fluids* 5:011501(R)

Shishkina O. 2020. Tenacious wall states in thermal convection in rapidly rotating containers. *J. Fluid Mech.* 898:F1

Shishkina O. 2021. Rayleigh–Bénard convection: the container shape matters. *Phys. Rev. Fluids* 6:090502

Shishkina O, Horn S, Wagner S. 2013. Falkner-Skan boundary layer approximation in Rayleigh–Bénard convection. *J. Fluid Mech.* 730:442–63

Shishkina O, Horn S, Wagner S, Ching ESC. 2015. Thermal boundary layer equation for turbulent Rayleigh–Bénard convection. *Phys. Rev. Lett.* 114:114302

Shishkina O, Stevens RJAM, Grossmann S, Lohse D. 2010. Boundary layer structure in turbulent thermal convection and its consequences for the required numerical resolution. *New J. Phys.* 12:075022

Shishkina O, Wagner S, Horn S. 2014. Influence of the angle between the wind and the isothermal surfaces on the boundary layer structures in turbulent thermal convection. *Phys. Rev. E* 89:033014

Spiegel EA. 1971. Convection in stars I. Basic Boussinesq convection. *Annu. Rev. Astron. Astrophys.* 9:323–52

Spiegel EA, Veronis G. 1960. On the Boussinesq approximation for a compressible fluid. *Astrophys. J.* 131:442–47

Sprague M, Julien K, Knobloch E, Werne J. 2006. Numerical simulation of an asymptotically reduced system for rotationally constrained convection. *J. Fluid Mech.* 551:141–74

Stellmach S, Hansen U. 2008. An efficient spectral method for the simulation of dynamos in Cartesian geometry and its implementation on massively parallel computers. *Geochem. Geophys. Geosyst.* 9(5):Q05003

Stellmach S, Lischper M, Julien K, Vasil G, Cheng JS, et al. 2014. Approaching the asymptotic regime of rapidly rotating convection: boundary layers versus interior dynamics. *Phys. Rev. Lett.* 113(25):254501

Stevens RJAM, Clercx HJH, Lohse D. 2010a. Boundary layers in rotating weakly turbulent Rayleigh–Bénard convection. *Phys. Fluids* 22:085103

Stevens RJAM, Clercx HJH, Lohse D. 2010b. Optimal Prandtl number for heat transfer in rotating Rayleigh–Bénard convection. *New J. Phys.* 12:075005

Stevens RJAM, Clercx HJH, Lohse D. 2012. Breakdown of the large-scale wind in aspect ratio $\Gamma = 1/2$ rotating Rayleigh–Bénard flow. *Phys. Rev. E* 86:056311

Stevens RJAM, Clercx HJH, Lohse D. 2013. Heat transport and flow structure in rotating Rayleigh–Bénard convection. *Eur. J. Mech. B* 40:41–49

Stevens RJAM, Overkamp J, Lohse D, Clercx HJH. 2011. Effect of aspect-ratio on vortex distribution and heat transfer in rotating Rayleigh–Bénard convection. *Phys. Rev. E* 84:056313

Stevens RJAM, Zhong JQ, Clercx HJH, Ahlers G, Lohse D. 2009. Transitions between turbulent states in rotating Rayleigh–Bénard convection. *Phys. Rev. Lett.* 103:024503

Stewartson K. 1957. On almost rigid rotation. *J. Fluid Mech.* 3:17–26

Taylor GI. 1921. Experiments with rotating fluids. *Proc. R. Soc. Lond. A* 100:114–21

Tilgner A. 2022. Bounds for rotating Rayleigh–Bénard convection at large Prandtl number. *J. Fluid Mech.* 930:A33

van Saarloos W, Hohenberg PC. 1992. Fronts, pulses, sources and sinks in generalized complex Ginzburg–Landau equations. *Physica D* 56:303–67

Veronis G. 1959. Cellular convection with finite amplitude in a rotating fluid. *J. Fluid Mech.* 5:401–35

Veronis G. 1962. The magnitude of the dissipation terms in the Boussinesq approximation. *Astrophys. J.* 135:655–56

Verzicco R, Camussi R. 2003. Numerical experiments on strongly turbulent thermal convection in a slender cylindrical cell. *J. Fluid Mech.* 477:19–49

Vogt T, Horn S, Aurnou JM. 2021. Oscillatory thermal–inertial flows in liquid metal rotating convection. *J. Fluid Mech.* 911:A5

Vorobieff P, Ecke RE. 2002. Turbulent rotating convection: an experimental study. *J. Fluid Mech.* 458:191–218

Wagner S, Shishkina O, Wagner C. 2012. Boundary layers and wind in cylindrical Rayleigh–Bénard cells. *J. Fluid Mech.* 697:336–66

Wang G, Santelli L, Lohse D, Verzicco R, Stevens RJAM. 2021. Diffusion-free scaling in rotating spherical Rayleigh–Bénard convection. *Geophys. Res. Lett.* 48(20):e2021GL095017

Wedi M, van Gils DP, Weiss S, Bodenschatz E. 2021. Rotating turbulent thermal convection at very large Rayleigh numbers. *J. Fluid Mech.* 912:A30

Wei P, Weiss S, Ahlers G. 2015. Multiple transitions in rotating turbulent Rayleigh–Bénard convection. *Phys. Rev. Lett.* 114:114506

Weiss S, Ahlers G. 2011a. Heat transport by turbulent rotating Rayleigh–Bénard convection and its dependence on the aspect ratio. *J. Fluid Mech.* 684:407–26

Weiss S, Ahlers G. 2011b. The large-scale flow structure in turbulent rotating Rayleigh–Bénard convection. *J. Fluid Mech.* 688:461–92

Weiss S, Ahlers G. 2011c. Turbulent Rayleigh–Bénard convection in a cylindrical container with aspect ratio $\Gamma = 0.50$ and Prandtl number $Pr = 4.38$. *J. Fluid Mech.* 676:5–40

Weiss S, He X, Ahlers G, Bodenschatz E, Shishkina O. 2018. Bulk temperature and heat transport in turbulent Rayleigh–Bénard convection of fluids with temperature-dependent properties. *J. Fluid Mech.* 851:374–90

Weiss S, Stevens RJAM, Zhong JQ, Clercx HJH, Lohse D, Ahlers G. 2010. Finite-size effects lead to supercritical bifurcations in turbulent rotating Rayleigh–Bénard convection. *Phys. Rev. Lett.* 105:224501

Weiss S, Wei P, Ahlers G. 2016. Heat-transport enhancement in rotating turbulent Rayleigh–Bénard convection. *Phys. Rev. E* 93(4):043102

Willoughby HE. 1990. Gradient balance in tropical cyclones. *J. Atmos. Sci.* 47:265–74

Xi HD, Lam S, Xia KQ. 2004. From laminar plumes to organized flows: the onset of large-scale circulation in turbulent thermal convection. *J. Fluid. Mech.* 503:47–56

Xi HD, Zhou Q, Xia KQ. 2006. Azimuthal motion of the mean wind in turbulent thermal convection. *Phys. Rev. E* 73:056312

Yang Y, Verzicco R, Lohse D, Stevens RJAM. 2020. What rotation rate maximizes heat transport in rotating Rayleigh–Bénard convection with Prandtl number larger than one? *Phys. Rev. Fluids* 5(5):053501

Zhang K, Roberts PH. 1997. Thermal inertial waves in a rotating fluid layer: exact and asymptotic solutions. *Phys. Fluids* 9:1980–87

Zhang X, Ecke RE, Shishkina O. 2021. Boundary zonal flows in rapidly rotating turbulent thermal convection. *J. Fluid Mech.* 915:A62

Zhang X, van Gils DPM, Horn S, Wedi M, Zwirner L, et al. 2020. Boundary zonal flow in rotating turbulent Rayleigh–Bénard convection. *Phys. Rev. Lett.* 124:084505

Zhong F, Ecke R, Steinberg V. 1991. Asymmetric modes and the transition to vortex structures in rotating Rayleigh-Bénard convection. *Phys. Rev. Lett.* 67(18):2473–76

Zhong F, Ecke R, Steinberg V. 1993. Rotating Rayleigh–Bénard convection: asymmetric modes and vortex states. *J. Fluid Mech.* 249:135–59

Zhong JQ, Ahlers G. 2010. Heat transport and the large-scale circulation in rotating turbulent Rayleigh–Bénard convection. *J. Fluid Mech.* 665:300–33

Zhong JQ, Stevens RJAM, Clercx HJH, Verzicco R, Lohse D, Ahlers G. 2009. Prandtl-, Rayleigh-, and Rossby-number dependence of heat transport in turbulent rotating Rayleigh–Bénard convection. *Phys. Rev. Lett.* 102:044502

Annual Review of Fluid Mechanics

Volume 55, 2023

Contents

Indexes

Errata

An online log of corrections to *Annual Review of Fluid Mechanics* articles may be found at http://www.annualreviews.org/errata/fluid